# WIYN Open Cluster Study. LXXXV. Li in NGC 2243: Implications for Stellar and Galactic Evolution

Barbara J. Anthony-Twarog <sup>1</sup> , Constantine P. Deliyannis <sup>2</sup> , and Bruce A. Twarog <sup>1</sup> Department of Physics and Astronomy, University of Kansas, Lawrence, KS 66045-7582, USA; bjat@ku.edu, btwarog@ku.edu 

<sup>2</sup> Department of Astronomy, Indiana University, Bloomington, IN 47405-7105, USA; cdeliyan@indiana.edu 

Received 2020 November 29; revised 2021 January 17; accepted 2021 January 26; published 2021 March 3

#### **Abstract**

High-dispersion spectra in the Li  $\lambda$ 6708 region have been obtained and analyzed in the old, metal-deficient cluster NGC 2243. From Hydra spectra for 29 astrometric and radial velocity members, we derive rotational velocities, as well as [Fe/H], [Ca/H], [Si/H], and [Ni/H] based on 17, 1, 1, and 3 lines, respectively. Using ROBOSPECT, an automatic equivalent width measurement program, we derive [Fe/H] =  $-0.54 \pm 0.11$  (MAD), for an internal precision for the cluster [Fe/H] below 0.03 dex. Given the more restricted line set, comparable values for [Ca/H], [Si/H], and [Ni/H] are  $-0.48 \pm 0.19$ ,  $-0.44 \pm 0.11$ , and  $-0.61 \pm 0.06$ , respectively. With E(B-V) = 0.055, appropriate isochrones imply  $(m-M) = 13.2 \pm 0.1$  and an age of  $3.6 \pm 0.2$  Gyr. Using available VLT spectra and published Li abundances, we construct an Li sample of over 100 stars extending from the tip of the giant branch to 0.5 mag below the Li dip. The Li dip is well populated and, when combined with results for NGC 6819 and Hyades/Praesepe, implies a mass/metallicity slope of  $0.4 M_{\odot}$ /dex for the high-mass edge of the Li dip. The A(Li) distribution among giants reflects the degree of Li variation among the turnoff stars above the Li dip, itself a function of stellar mass and metallicity and strongly anticorrelated with a  $v_{\rm rot}$  distribution that dramatically narrows with age. Potential implications of these patterns for the interpretation of Li among dwarf and giant field populations, especially selection biases tied to age and metallicity, are discussed.

Unified Astronomy Thesaurus concepts: Open star clusters (1160); Stellar abundances (1577)

#### 1. Introduction

With improved precision and rapidly expanding databases due to the application of larger telescopes in survey mode (see, e.g., Casali et al. 2019; Gao et al. 2019), the abundance of atmospheric Li (A(Li)<sup>3</sup>) has become an increasingly valuable signature of both stellar structure and galactic chemical evolution. Since lower-mass main-sequence and red giant stars represent a crucial interface between both research areas, an extensive spectroscopic program has been underway to survey members of a key set of open clusters from the tip of the giant branch to as far down the main sequence as the technology allows. New spectroscopy and/or reanalyses of published data have been discussed for NGC 752, NGC 3680, and IC 4651 (Anthony-Twarog et al. 2009), NGC 6253 (Anthony-Twarog et al. 2010; Cummings et al. 2012), NGC 2506 (Anthony-Twarog et al. 2016, 2018), Hyades and Praesepe (Cummings et al. 2017), NGC 6819 (Anthony-Twarog et al. 2014; Lee-Brown et al. 2015; Deliyannis et al. 2019, hereafter referred to as D19), and, most recently, NGC 188 (Sun et al. 2020). The regularly repeated rationale for investigation of these clusters and their role within the bigger picture of Li evolution can be found in the respective papers and will not be detailed here. An overview of the goals and some current insight into the benefits of a more comprehensive approach to open cluster analyses can be found in Twarog et al. (2020).

The focus of this investigation is the metal-deficient, older open cluster NGC 2243. Just how metal-deficient the cluster is will be a point we return to in Section 3. There is, however, long-standing agreement that, irrespective of the technique used to derive the metallicity and/or the exact zero-point of the metallicity scale, when ranked by metallicity among the well-

studied open clusters within 5 kpc of the Sun, NGC 2243 sits consistently at or near the bottom of the list (Twarog et al. 1997; Friel et al. 2002; Netopil et al. 2016). This combination of distance, metallicity, and an age competitive with that of M67 (see Section 4) makes NGC 2243 an important test bed for the effects of metallicity on the rate and degree of Li evolution among lower-mass stars while on the main sequence and, to an even greater extent, in subgiant and giant branch phases. Isolating the metallicity-dependent effects of atmospheric evolution also allows exposure of the underlying patterns of Galactic Li evolution at both the metal-poor and metal-rich ends of the scale (Randich et al. 2020). Moreover, for now, the main-sequence stars provide one of the closest links to their analogs within the halo population and a constraint on the apparent contradiction between stellar and cosmological predictions for the primordial A(Li) (Spite Spite 1982a, 1982b).

In an attempt to expand the spectrosopic sample over the full range of luminosity from the tip of the red giant branch to the main sequence below the Li dip (Boesgaard & Tripicco 1986), our own Hydra data, detailed in Section 2, have been supplemented when possible by high-resolution spectra obtained at the VLT, and by reconsidered A(Li) from published sources when no spectra were accessible. The layout of the discussion is as follows: Section 2 details the new spectra; their processing, reduction, and velocity derivation; the additional spectra from other sources; and a compilation of precision broadband photometry for color-magnitude diagram (CMD) analysis. Section 3 lays out the cluster metallicity determination from the Hydra spectra and comparison with previous results. Section 4 combines the metallicity, reddening, and BV CMD to define the cluster age and distance, and indirectly the masses of the stars populating the turnoff and giant branch, through comparison to appropriate isochrones. Section 5 describes the

<sup>&</sup>lt;sup>3</sup>  $A(Li) = log N_{Li} - log N_H + 12.00.$ 

Li abundance estimation for new members within the Hydra and VLT samples and combines these with previously published determinations to delineate the evolutionary trend within the cluster and place the cluster within the context of Li changes with both age and metallicity. Section 6 summarizes our results for NGC 2243 while illuminating the impact of the varying boundaries of the Li dip due to metallicity effects on our understanding of Galactic Li evolution and selection bias.

#### 2. Observational Data: New, Old, and Revisited

# 2.1. Spectroscopy: WIYN Hydra Data—Acquisition and Reduction

NGC 2243 is a compact cluster, and while it is rather far south for northern hemisphere observations, access to the Hydra multiobject spectrograph on the WIYN 3.5 m telescope<sup>4</sup> motivated spectroscopic observations in this critical cluster.

Our candidate list of cluster members was constructed long before Gaia DR2 (Gaia Collaboration et al. 2018a) and was based primarily on analyses of precision extended Strömgren photometry (Anthony-Twarog et al. 2005) (ATAT) using the traditional intermediate- and narrowband indices of the system. Under the assumption that cluster members should exhibit similar chemical composition and reddening, we additionally compiled a new parameter H, defined as hk - 2.25(b - y), and compared this photometric construct to then-current membership information, mainly radial velocities. H values for the most likely member candidates centered on -0.40; any star that deviated significantly from this target figure was eliminated as a spectroscopic target. Table 1 lists basic information about our Hydra sample, including coordinates, WEBDA<sup>5</sup> identification numbers, and V and B-V photometry compiled as described below. All of the stars above the dividing horizontal line in Table 1 are judged members by Cantat-Gaudin et al. (2018) based on Gaia DR2 astrometry. Additional data about each star's rotational and radial velocities are presented, with further descriptions to follow.

Two Hydra fiber configurations were constructed, one with nine bright stars and another with an eventual total of 33 fainter targets designed for longer, multiple exposures. The brighter configuration was observed for three 30-minute exposures on 2015 January 21, where the date indicates the UT date. Stars in the fainter configuration were observed with exposures ranging from 53 to 90 minutes, for 180 minutes total on 2015 January 21, 268 minutes on 2015 January 22, and 246 minutes on 2016 January 12, amounting to 11.6 hr of total exposure. Between the 2015 and 2016 runs, one fiber fell out of use so that one star, observed only in 2015, was replaced by another star observed only in 2016; the other 31 stars were observed in both years. Notes to Table 1 indicate which stars were observed in only one epoch.

Our spectrograph setup is designed to cover a wavelength range  $\sim 400 \,\text{Å}$  centered on 6650 Å, with dispersion of 0.2 Å pixel<sup>-1</sup>. Examination of thorium-argon lamp spectra indicates a line resolution comprising 2.5 pixels, yielding a spectral

resolution over 13,000. The data were subsequently processed using standard reduction routines in IRAF,<sup>6</sup> including, in order of application, bias subtraction, division by the averaged flat field, dispersion correction through interpolation of the comparison lamp spectra, throughput correction for individual fibers using daytime sky exposures in the same configuration, and continuum normalization. After flat-field division and before the dispersion correction, the long-exposure program images were cleaned of cosmic rays using "L. A. Cosmic" (van Dokkum 2001). Real-time sky subtraction was accomplished by using the dozens of fibers not assigned to stars and exposed to the sky during each integration.

Cumulative spectra for each configuration were constructed by additive combination by night and by year; the differences between 2015 and 2016 values were also examined for signs of potential radial velocity variation before construction of cumulative combination spectra. Other than WEBDA 2135 (W2135), discussed in detail in Anthony-Twarog et al. (2020, hereafter Paper I), no other stars show significant variation between the two epochs. The signal-to-noise ratio (S/N) per pixel has been estimated by direct inspection of the composite spectra within IRAF's SPLOT utility, using mean values and rms scatter from a relatively line-free region between 6680 and 6694 Å. S/N estimates of Table 1 characterize the summed composite spectra, with a median value of 138 achieved for the sample.

#### 2.2. Spectroscopy: VLT Data

Largely because early analyses indicated a fascinating range of anomalies for member giant W2135 (Paper I), we sought to expand our sample of spectroscopically observed stars by searching for archival spectra within the field of NGC 2243 and with spectral coverage in the region of the Li line. We gratefully acknowledge use of the ESO Science Archive Facility, from which we retrieved fully processed spectra obtained for the public Gaia ESO Survey at the Very Large Telescope (VLT) with the Fibre Large Array Multi Element Spectrograph (FLAMES) fiber-feed assembly to both the highresolution UVES spectrograph and the GIRAFFE spectrograph, with pixel resolutions of 16.9 and 50 mÅ, respectively. As our intention was to use these spectra for Li abundance analysis only, we performed no further processing other than to import them to a format acceptable to standard IRAF routines. The higher resolution of the VLT spectra, particularly those from the UVES instrument, provides a considerable advantage for Li analysis, although S/N above 100 is still desirable even for higher-resolution spectra. Our initial archive search was limited to spectra described as having S/N above 70; where possible, multiple exposures were co-added to produce spectra with higher S/N.

As a result, additional spectra for some of the stars listed in Table 1 were found and examined to take advantage of the higher resolution of the VLT spectra. Notes to Table 1 indicate the Hydra sample stars for which VLT spectra were also examined. VLT spectra for 11 probable member stars not included in the Hydra sample were also identified. Table 2

<sup>&</sup>lt;sup>4</sup> The WIYN Observatory was a joint facility of the University of Wisconsin–Madison, Indiana University, Yale University, and the National Optical Astronomy Observatory.

https://webda.physics.muni.cz

<sup>&</sup>lt;sup>6</sup> IRAF is distributed by the National Optical Astronomy Observatory, which is operated by the Association of Universities for Research in Astronomy, Inc., under cooperative agreement with the National Science Foundation.

http://www.astro.yale.edu/dokkum/lacosmic/, an IRAF script developed by P. van Dokkum (van Dokkum 2001); spectroscopic version.

http://archive.eso.org/scienceportal

Table 1
Stellar Characteristics, Hydra Sample

WEBDA ID	$\alpha(2000)$	δ(2000)	V	B-V	S/N	$V_{\rm rad}$	$\sigma_{ m Vrad}$	$v_{\rm rot}$	$\sigma_{ m vrot}$	Note
					$(pixel^{-1})$	$V_{\rm rad}$ (km s <sup>-1</sup> )	$(\text{km s}^{-1})$	$(\text{km s}^{-1})$	$\frac{\sigma_{\rm vrot}}{({\rm km~s}^{-1})}$	
519	97.307140	-31.350243	15.724	0.524	157	55.54	1.89	16.54	1.03	
611	97.317848	-31.279542	15.384	0.861	185	55.67	1.64	11.92	0.69	a
716	97.327288	-31.225097	15.731	0.504	154	44.64	2.18	19.56	1.32	
873	97.342210	-31.281069	15.712	0.557	164	55.20	1.35	8.86	0.43	
1044	97.357060	-31.273251	15.702	0.493	135	53.16	2.13	13.56	0.93	
1133	97.362952	-31.307905	16.074	0.497	60	39.72	3.60	31.96	2.82	a
1230	97.369157	-31.205316	15.996	0.744	153	54.80	1.57	11.96	0.67	
1263	97.372145	-31.295469	15.241	0.807	196	55.74	1.70	21.76	1.10	a
1266	97.372710	-31.366009	15.662	0.549	124	54.74	1.84	14.65	0.92	a
1271	97.372511	-31.262745	13.692	0.918	132	56.95	0.73	11.70	0.29	a,b
1294	97.374103	-31.273084	15.472	0.861	127	56.16	1.38	11.23	0.44	a,b
1313	97.375413	-31.282930	12.887	1.097	124	57.51	0.72	4.65	0.12	a,c
1421	97.381966	-31.259343	15.868	0.826	153	55.82	2.17	14.84	1.07	
1436	97.382878	-31.301186	15.823	0.480	134	53.69	2.18	19.17	1.32	
1467	97.385029	-31.291483	13.713	0.930	130	56.12	0.83	15.61	0.44	a,b
1696	97.396588	-31.289930	14.201	0.965	199	57.63	1.24	11.96	0.52	
1738	97.398569	-31.286365	13.721	0.925	129	56.64	0.86	18.95	0.51	b
1847	97.403533	-31.245067	14.219	0.962	164	58.18	1.34	16.23	0.72	
1871	97.405196	-31.318901	15.485	0.482	159	55.34	1.89	15.36	0.96	
1995	97.412396	-31.287251	15.909	0.824	127	54.79	1.47	10.94	0.55	
2003	97.412831	-31.299608	15.731	0.469	138	53.36	2.99	21.70	1.91	
2098	97.417557	-31.247321	15.884	0.707	129	56.00	1.47	11.14	0.55	
2135	97.421203	-31.318307	13.802	1.072	315		1.67	38.77	1.54	a,d
2394	97.439450	-31.250351	15.726	0.540	137	55.30	2.57	13.01	1.37	
2410	97.440970	-31.260588	13.633	0.936	105	58.43	0.90	12.67	0.39	a,b
2434	97.442601	-31.267117	14.076	0.821	248	55.42	1.34	11.73	0.54	
2676	97.464961	-31.303919	15.996	0.452	123	53.02	2.19	12.76	1.00	
2696	97.466663	-31.238735	16.007	0.451	130	54.05	3.07	20.15	1.85	
2908	97.488997	-31.267521	16.021	0.455	113	56.42	2.84	20.71	1.80	
3618	97.422947	-31.243319	13.683	1.046	107	56.60	0.71	11.54	0.27	a,b
3633	97.368411	-31.288134	12.025	1.418	81	57.11	1.07	13.13	0.46	a,b
3728	97.295890	-31.344250	13.316	0.992	119	57.79	0.96	19.58	0.59	a,b
259	97.272604	-31.284006	14.714	0.957	175	58.33	1.20	9.70	0.41	
507	97.305208	-31.280300	12.112	1.048	130	80.21	0.88	9.01	0.28	b
552	97.310604	-31.234522	14.820	0.508	249	46.93	1.21	12.58	0.55	
718	97.327242	-31.188708	15.862	0.519	149	74.54	3.00	22.14	2.17	
2451	97.444504	-31.384656	13.985	0.594	248	-13.58	1.94	13.93	1.07	
2528	97.450467	-31.324308	15.736	0.539	121	67.83	2.44	24.58	1.67	
2704	97.467308	-31.281325	15.070	0.967	203	3.74	1.84	16.44	0.98	
2719	97.468896	-31.359297	13.881	0.531	282	3.90	1.62	17.18	0.92	
3063	97.510746	-31.266553	15.284	0.560	147	45.06	1.41	15.04	0.78	
3726	97.304417	-31.309617	11.576	1.166	36	117.27	1.10	10.39	0.39	b

#### Notes

presents the basic information for these stars, comparable to that presented for the Hydra stars in Table 1, although radial and rotational velocity values have not been estimated for the VLT spectra; in the place of these data, atmospheric parameters used in later analysis steps are included in this table. S/N values are reproduced from the processed spectra's headers or report quadratic sums for co-added spectra. Direct measurements of the S/N between 6680 and 6694 Å largely confirm these listed values as adequate representation of the S/N per pixel.

# 2.3. WIYN Hydra Data: Radial and Rotational Velocities

We utilized the *fxcor* Fourier-transform, cross-correlation utility in IRAF to assess velocities for each star in each year's composite spectra. In *fxcor*, stars are compared to a stellar template of similar  $T_{\rm eff}$  for the wavelength range of our spectra redward of  $H\alpha$ . Output of the *fxcor* utility characterizes the cross-correlation function (CCF), from which estimates of each star's radial velocity are easily inferred.

From the procedure for radial velocity estimation, rotational velocities can also be estimated from the CCF FWHM using a procedure developed by Steinhauer (2003). This procedure exploits the relationship between the CCF FWHM, line widths,

<sup>&</sup>lt;sup>a</sup> Li analysis from additional VLT spectra.

b Radial velocity obtained from only 2015 spectra.

<sup>&</sup>lt;sup>c</sup> Radial velocity obtained from only 2016 spectra.

 $<sup>^{\</sup>rm d}$  Radial velocity for W2135 was 39.7 km s $^{-1}$  in 2015 and 74.4 km s $^{-1}$  in 2016.

Table 2	
Stellar Characteristics,	VLT Sample

WEBDA ID	$\alpha(2000)$	δ(2000)	V	B-V	S/N	$T_{ m eff}$	log g	ξ
239	97.269875	-31.357306	13.644	0.891	94	4990	2.5	1.50
365	97.288917	-31.175694	14.009	0.975	151	4824	2.5	1.50
910	97.345833	-31.291639	13.717	0.916	196	4939	2.5	1.50
1261	97.372208	-31.359833	15.177	0.873	130	5027	3.1	1.39
1679	97.395958	-31.322167	15.113	0.874	99	5025	3.1	1.39
1686	97.396333	-31.338639	15.675	0.496	130	6324	3.8	1.81
1923	97.408167	-31.276917	15.838	0.449	114	6538	3.9	1.97
2195	97.424500	-31.263194	15.321	0.766	133	5267	3.2	1.41
2536	97.451542	-31.377111	15.234	0.892	135	4987	3.1	1.38
2613	97.458250	-31.278306	15.146	0.828	94	5124	3.1	1.41
2648	97.462536	-31.245210	14.449	0.942	88	4888	2.75	1.50

and  $v_{\rm rot}$ , using a set of numerically "spun-up" standard spectra with comparable spectral types to constrain the relationship. Our analyses of both red giant and turnoff spectra demonstrate that *fxcor* cross-correlation profiles have significantly reduced accuracy when attempting to reproduce rotational velocities above  $30~{\rm km~s^{-1}}$ . Our spectral resolution implies that rotational velocities below  $10~{\rm km~s^{-1}}$  are not meaningful.

Radial and rotational velocities for each of our program stars are included in Table 1, divided into likely members and nonmembers based on Gaia astrometry. Listed errors reflect the precision of the template fit by fxcor. As noted earlier, the lines of Table 1 are separated by astrometric membership categories applied after sample selection and data acquisition. The top 32 stars are considered members in the compilation by Cantat-Gaudin et al. (2018) based on Gaia DR2 astrometry, while the bottom 10 stars, initially selected by photometric criteria to be potential members, are now designated as unlikely astrometric members. In nearly every case, our radial velocity information for the 10 likely nonmembers is consistent with the astrometric classification. The exception is star W259, for which DR2 astrometry indicates a parallax  $\sim 1/2$  the cluster average value and a total proper motion  $\sim 1/3$  the magnitude of the cluster motion (Cantat-Gaudin et al. 2018). In addition to the 10 astrometric nonmembers, stars W2135, W1133, and W716 have been excluded from the computation of the average cluster radial velocity for reasons addressed below. An average radial velocity from the most likely members is  $55.8 \pm 1.5 \,\mathrm{km \, s^{-1}}$ , where the error statistic is the standard deviation among the 29 stars.

Star W2135 has been discussed in detail in Paper I. In summary, in addition to a measurable (and therefore distinctive for the cluster's age and the star's evolutionary state) Li line, this giant had been flagged as a photometric variable by ATAT and as V14 by Kaluzny et al. (2006a). Limited information regarding photometric amplitude or periodicity emerged from either photometric study, beyond a period estimated in days rather than hours. From Hydra spectra, we were only able to note a significant change in radial velocity between our two observational epochs, from 39.7 km s<sup>-1</sup> in 2015 to 74.4 km s<sup>-1</sup> 1 yr later, for an average fortuitously near the cluster mean. Our velocity analyses indicated abnormally large  $v_{\rm rot}$  sin i for a giant star, at least  $40 \, {\rm km \, s^{-1}}$ , although we note again that analysis of the fxcor cross-correlation profiles probably cannot accurately reproduce rotational velocities above  $\sim 30 \, {\rm km \, s^{-1}}$ .

Reiterating a note added in proof to Paper I, the All-Sky Automated Survey for SuperNovae (ASAS-SN) variable stars database (Shappee et al. 2014)<sup>9</sup> includes star W2135. The cataloged star, ASASSN-V J062941.11-311906.9/V0412 CMa, has a variability class of ROT, implying that the variability is likely due to rotationally induced brightness modulation, with a period of 6.755421 days (Jayasinghe et al. 2019). Thus, the estimated true  $v_{\rm rot}$ , i.e., with the sin i effect removed, using stellar parameter estimates derived from the CMD location of the star becomes  $86\,{\rm km\,s^{-1}}$  (Paper I).

The spectra for W1133 are essentially featureless other than  $H\alpha$ , indicating either a higher temperature than suggested by the star's color, rapid rotation, or both. This star is also a variable candidate from Kaluzny et al. (2006a) (V13), with a tentative classification as a  $\gamma$  Doradus variable and a period of  $\sim$ 0.77 days. We were unable to obtain *fxcor* results for one of the two epochs and consider its one radial velocity determination tentative. Star W716 had a consistent radial velocity indicative of nonmembership for both epochs, in spite of a classification as a highly probably member based on astrometry. If a cluster member, it must be a single-lined spectroscopic binary (SB1), and we were unlucky in our phase sampling, a result confirmed below.

#### 2.4. Comparison with Other Radial Velocity Determinations

A few radial velocity standards were observed on some, but not all, of the 2015 and 2016 nights on which NGC 2243 was observed. Our radial velocities derived from fxcor analysis yield  $V_{\rm rad}$  that are, on average,  $0.6 \pm 0.7 \, {\rm km \, s}^{-1}$  too large in comparison to the velocities quoted for our adopted standards on the SIMBAD database. Although the absolute scale of our radial velocities was considered less critical than the internal or relative values for purposes of confirming common membership or detecting SB candidates, there are several radial velocity surveys of NGC 2243 with which we can compare our mean results, even though the direct overlap in stellar samples is significant for only two surveys. Comparisons of the radial velocities of overlapping stars to other past surveys have been constructed and are summarized in Table 3.

François et al. (2013, hereafter FR13) derive a cluster mean radial velocity of 61.9 km s<sup>-1</sup>, some 6.1 km s<sup>-1</sup> higher than our Hydra-based result of +55.8 km s<sup>-1</sup> from the 29 member stars. Only one star is common to both studies, the likely nonmember

<sup>9</sup> https://asas-sn.osu.edu/variables

<sup>&</sup>lt;sup>10</sup> Operated at CDS, Strasbourg, France (Wenger et al. 2000), http://simbad.u-strasbg.fr/simbad.

Table 3
Radial Velocity Comparisons: Table 1—LIT

Survey	$\Delta(V_{\rm rad})$ (km s <sup>-1</sup> )	$(\text{km s}^{-1})$	Number of Stars
Gaia DR2	-1.7	1.3	6
Gaia 3D	-4.2	1.8	24
FR13	-5.2		1
JFP	0.2	1.3	12
Gratton	-3.7	1.1	2
Mermilliod	-2.9		1
FJ93	-8.2	10.4	4
FR02	-4.1	12.4	7
Kaluzny	2.8		1
Minitti	2.8	9.6	7
Cameron & Reid	-16.9	9.9	5

Note. DR2: Gaia Collaboration et al. (2018a); G3D: Jackson et al. (2020); FR13: François et al. (2013); JFP: Jacobson et al. (2011); Gratton (1982); Mermilliod et al. (2008); FJ93: Friel & Janes (1993); FR02: Friel et al. (2002); Kaluzny: Kaluzny et al. (1996); Minitti (1995); Cameron & Reid (1987).

W552; our derived radial velocity is  $5.2~\rm km~s^{-1}$  smaller than that quoted by FR13. The most recent, and largest, analysis of motions in the cluster by Jackson et al. (2020) (G3D) indicates a cluster velocity of  $59.82 \pm 0.58~\rm km~s^{-1}$ , again larger than our average value by  $4.2~\rm km~s^{-1}$ , where the quoted error reflects only the internal dispersion within the cluster.

We have referred to the G3D analysis to reevaluate the membership credentials of stars described in Tables 1 and 2 (Hydra and VLT samples), as well as samples reported on by FR13 and Hill & Pasquini (2000) (HP). Referring once again to stars excluded from our Hydra radial velocity analysis, radial velocity discrepancies for stars W2135, W1133, and W716 are confirmed. In Table 1,  $V_{\rm rad}$  for W716 is noted as 44.6 km s<sup>-1</sup>, quite a bit lower than the internal average for the cluster of 55.8 km s<sup>-1</sup>. Results from G3D indicate a radial velocity of 68.3 km s<sup>-1</sup>, but likely membership, suggesting even more strongly an SB1 nature for this star. The situation is much the same for W1133, known to be a variable and potential binary; the G3D  $V_{\rm rad}$  is even lower than the 39.7 km s<sup>-1</sup> listed in Table 1. Finally, W2135 exhibits a G3D radial velocity of 80.4 km s<sup>-1</sup>, similar to our larger 2016 measurement and further confirmation of its SB character.

# 2.5. Photometry and Reddening

Reliable photometry plays a dual role in the discussion of NGC 2243. When adjusted for metallicity and reddening, it (a) is the basis for deriving the  $T_{\rm eff}$  used in spectroscopic abundance estimation and (b) permits age and distance determination through comparison to appropriate isochrones, leading to mass estimates for individual stars at a variety of CMD positions. A comprehensive discussion of the broadband BV photometry available at the time can be found in ATAT. For NGC 2243, only two significant CCD BV surveys of the cluster were then available (Bonifazi et al. 1990; Bergbusch et al. 1991), focusing on the central region of the cluster owing to smaller-format CCDs. Fortunately, comparison of the two data sets showed excellent agreement, indicating that both were well tied to the standard BV system at the time as defined by Landolt (1983) and Graham (1982). The merger of these two photometric sets is described in detail in ATAT and will not be

repeated. Somewhat surprisingly, with the exception of the Gaia DR2 data set, no wide area broadband studies, BV or otherwise, have been added to the literature since then.

For our purposes the photometric compilation has been broken down into two distinct regions, the red giants  $((B-V) \ge 0.70)$  and the turnoff region ((B-V) < 0.70)through the unevolved main-sequence stars to  $V \sim 18.5$ . For the red giants, the primary photometric data set is the precision uvbyCaH\beta CCD photometry of ATAT. ATAT used the multicolor indices to identify highly probable cluster members and to convert the high-precision (V, b - y) for likely members to the traditional (V, B - V) system defined by the earlier, smaller CCD samples (Bergbusch et al. 1991; Bonifazi et al. 1990). As detailed in Paper I, the Gaia DR2  $(G, B_p - R_p)$ photometry for the red giants was readily transferred to the (V,B-V) system using 25 member giants (Cantat-Gaudin et al. 2018) in common, with the scatter in residuals between the two systems measured at  $\pm 0.007$  and  $\pm 0.009$  mag in V and (B-V), respectively. This allowed a merger of the two photometric data sets and reliable expansion of the BV system for giants to Gaia DR2 members outside the field studied by ATAT. As detailed in Paper I, this leads to 39 red giant members in the color range of interest.

For the turnoff and main-sequence stars, only the merged (V, B-V) data of Bergbusch et al. (1991) and Bonifazi et al. (1990) were adopted for stars within the survey areas. For a small subsample of stars far enough beyond the cluster core to lie outside the coverage of both BV surveys, simple  $(G, B_p - R_p)$  transformations to (V, B-V) with linear terms in  $(B_p - R_p)$  were defined using only astrometric members of the cluster (Cantat-Gaudin et al. 2018) within the same magnitude range as the stars of interest at the turnoff. Unlike the multiple merger process for broadband and intermediate-band photometry applied to the giants, the transformed Gaia data were adopted only for the stars not found within the BV CCD surveys.

A comprehensive discussion of the cluster reddening as of 2005 is given in ATAT. An early photometric study by Kaluzny et al. (1996) used VI photometry to obtain a reddening estimate E(V-I) = 0.10, implying E(B-V) = 0.077 using E (V-I) = 1.35\*E(B-V). This estimate depends in part on analysis of a nearby field RR Lyr, which permits setting 0.08 as an upper limit for E(B-V). We note, however, that Kaluzny et al. (2006b), in their analysis of the eclipsing binary (EB) NV CMa, adopt the ATAT reddening value and an [Fe/H] similar to the value obtained therein to derive their EB mass, cluster distance, and age estimates. From the extended Strömgren photometry of 100 stars at the turnoff, ATAT derived E  $(B-V) = 0.055 \pm 0.004$  (sem). At the time, the only other estimate with reasonable precision was that of Schlegel et al. (1998) with E(B-V) = 0.074, the maximum value along the line of sight in the direction of the cluster. Using the online tool, more recent corrections to the earlier reddening maps (Schlafly & Finkbeiner 2011) have reduced this value to a maximum reddening of  $0.058^{+0.011}_{-0.005}$  in the direction of NGC 2243. Unfortunately, NGC 2243 sits at the edge of the map generated by Green et al. (2019), and attempts to derive the trend along the line of sight fail to converge.

Finally, in Figure 1 we illustrate the location of the stars under discussion within the CMD of NGC 2243. Filled black

<sup>11</sup> https://irsa.ipac.caltech.edu/applications/DUST/

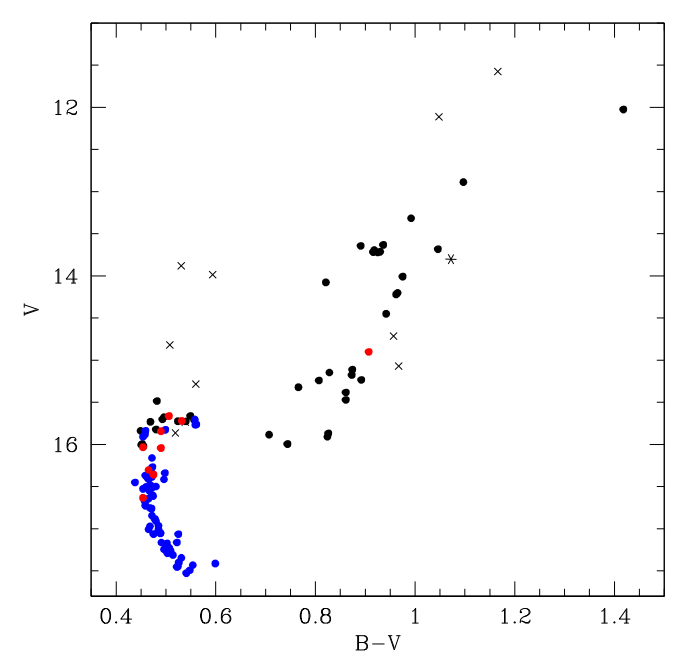


**Figure 1.** CMD of stars with Li spectroscopy. Filled black circles and crosses are the members and nonmembers, respectively, from Tables 1 and 2. Filled blue circles are the members from FR13, and the filled red circles are members from HP. W2135 is noted with an asterisk symbol.

circles and crosses are the members and nonmembers, respectively, from the combined samples of Tables 1 and 2. An asterisk notes the location of W2135. Filled blue circles are the members from FR13, and the filled red circles are members from HP. Of the 10 identified nonmembers, only two near the top of the turnoff fall within the CMD trend defined by the cluster members. Four nonmembers populate the blue straggler region well above the turnoff, and the other four occupy the red giant zone, again well off the track defined by the members.

A few stars considered members by FR13 and HP are not included in this plot or in further analysis, due to ambiguous or missing astrometric information. These include W3628 (referred to as 1035 by François et al. 2013, using the second of two numbering schemes introduced by Kaluzny et al. 1996) and W2512 (1106). An additional star, W1910, from the HP sample has also been excluded from further consideration.

FR13 provide no additional information about the stars they identify as probable nonmembers based on radial velocities, but note that one star, Kaluzny 1410 (W2363), has an essentially featureless spectrum, so much so that no  $V_{\rm rad}$  estimate is possible. This description bore a striking resemblance to the appearance of the Hydra spectrum for W1133; we were prompted to verify that like W1133, W2363 has been identified as variable star V3 by Kaluzny et al. (2006a), an eclipsing binary NW CMa of W UMa class with a period of 0.356 days. Although confirmed as an astrometric member by Cantat-Gaudin et al. (2018), the star is not included in the G3D sample, presumably because of a lack of a reliable  $V_{\rm rad}$  measurement.

#### 3. Abundance Analysis: Hydra Spectra

# 3.1. Spectroscopic Processing with ROBOSPECT

As described in Lee-Brown et al. (2015), we have employed the automated equivalent width (EW) measuring software ROBOSPECT (Waters & Hollek 2013). Details (Lee-Brown

et al. 2015) are provided of our tests of the software and refinement of a line list to exploit the iron and other heavy-element lines included in the  $\sim$ 400 Å region surrounding the Li line. For the present investigation, we utilize the line list refined in that paper, which includes 17 Fe, 1 Ca, 1 Si, and 3 Ni lines.

In addition to the potential members of NGC 2243, daytime sky spectra were obtained in 2015 and 2016 using the identical Hydra fiber configuration and wavelength coverage. These spectra were analyzed using ROBOSPECT and used to reference the abundance from each line to the solar value by implementing minor adjustments, if necessary, to log gf values for any line. This approach ensures that our abundances are relative to the solar value and solar spectrum rather than any adopted solar abundance value. From all ROBOSPECT output, we discarded negative EW (ROBOSPECT's designation of emission lines) owing to nonconvergent fitting solutions, artifacts of cosmic-ray removal, large noise spikes, or nonexistent lines in the measured spectrum. We also excluded measured EW below 5 mÅ or above 150 mÅ.

# 3.2. T<sub>eff</sub> Surface Gravity, and Microturbulent Velocity

From measured EW, abundances are derived in the context of a stellar atmosphere model constructed with appropriate values of  $T_{\rm eff}$ , log g, and microturbulent velocity  $\xi$ . The  $T_{\rm eff}$  determination was approached in a manner to ensure consistency with previous spectroscopic studies by this group. For dwarfs, we continue to use the calibration defined in Deliyannis et al. (2002); for giants, the  $T_{\rm eff}$ -color-[Fe/H] calibration of Ramírez & Meléndez (2005) was used. In both regimes, reddening values of E(B-V)=0.055 were applied to E(B-V)=0.055 adopted in the color-temperature calibration.

Estimates of the surface gravity were obtained for each likely member star in our spectroscopic sample by comparing its V, B-V values to a Victoria-Regina isochrone (VandenBerg et al. 2006) (VR), constructed with the appropriate age, metallicity, and corrections for distance and reddening, as discussed in Section 4. Our approach to microturbulent velocity estimation follows the one used in Lee-Brown et al. (2015). For stars with surface gravity below 3.0,  $\xi$  was estimated using a surface-gravity-based algorithm,  $\xi = 2.0 - 0.2 \log g$ . For less evolved stars, we employ the  $T_{\rm eff}$ ,  $\log g$  formulation developed by Bruntt et al. (2012), based on comparison of spectroscopic and asteroseismic parameters for Kepler stars.

Model atmospheres were constructed for each program star using the grid of Kurucz (1995) with input  $T_{\rm eff}$ , log g, and microturbulent velocity values. Each star's measured EWs and model serve as input to the *abfind* routine of MOOG (Sneden 1973) to produce individual [A/H] estimates for each successfully measured line in each star. With high confidence in the membership credentials for our spectroscopic sample, it makes sense to follow the statistical approach outlined in Lee-Brown et al. (2015), including the consistent use of medians to estimate cluster values, as well as constructed median absolute deviation (MAD) statistics to estimate the range for each estimated quantity.

Figure 2 illustrates information presented in Table 4, including the [A/H] values obtained from each of the 22 lines in our line list; error bars indicate the MAD statistic for abundance values derived from metal lines in as many as 29 stars (or as few as 14). Clearly, some lines produce noisier results than others, but we stress that use of median estimators

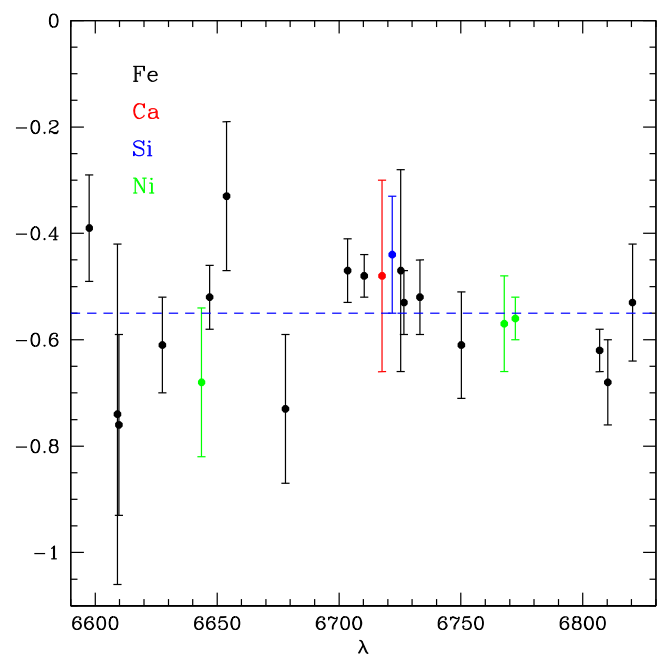


Figure 2. Median abundances and MAD statistics for each analyzed line in Hydra spectra.

Table 4
Characteristics and Results for Individual Metal Lines

Elem.	λ (Å)	[A/H]	Number of Stars	MAD
Fe	6597.56	-0.39	25	0.10
Fe	6609.11	-0.74	23	0.32
Fe	6609.68	-0.76	20	0.17
Fe	6627.54	-0.61	22	0.09
Fe	6646.93	-0.52	14	0.06
Fe	6653.91	-0.33	14	0.14
Fe	6677.99	-0.73	20	0.14
Fe	6703.57	-0.47	24	0.06
Fe	6710.32	-0.48	18	0.04
Fe	6725.36	-0.47	17	0.19
Fe	6726.67	-0.53	25	0.06
Fe	6733.15	-0.52	20	0.07
Fe	6750.15	-0.61	28	0.10
Fe	6806.86	-0.62	21	0.04
Fe	6810.27	-0.68	24	0.08
Fe	6820.37	-0.53	23	0.11
Fe	6837.01	-0.44	16	0.19
Ca	6717.68	-0.48	25	0.18
Si	6721.85	-0.44	28	0.11
Ni	6643.63	-0.68	28	0.14
Ni	6767.77	-0.57	29	0.09
Ni	6772.31	-0.56	27	0.04

lessens the impact of these lines. The dashed horizontal line indicates an overall [Fe/H] value of -0.55, based on the following considerations. Perhaps the most robust statistical estimation of the cluster's [Fe/H] is derived from the median of all 354 line measures, with a resulting median value of [Fe/H] = -0.55 and an MAD of 0.13 dex for all 354 separate estimators of [Fe/H]. An approximation of a standard deviation for our sample is given by 1.48\*MAD, or 0.19.

Consideration of the [Fe/H] values for each of the 17 Fe lines leads to a median value of [Fe/H] = -0.53 among the 17 estimations, MAD = 0.10 dex, and an estimated standard

deviation of 0.15. Taking the 29 separate [Fe/H] estimations for the sample stars, a median value of [Fe/H] = -0.56 is obtained, MAD = 0.12 dex, and  $\sigma = 0.18$ . As a precaution, we recomputed this median using only stars with at least eight successfully measured Fe lines, producing the same result.

From a consistency standpoint, this result is encouraging. ATAT derived a weighted average of  $[Fe/H] = -0.57 \pm 0.03$  (sem) from  $m_1$  and hk for 100 stars at the NGC 2243 turnoff, slightly lower than the typical result above. For NGC 2506, analyzed in the same manner as NGC 2243, Anthony-Twarog et al. (2018) derived a spectroscopic abundance of  $[Fe/H] = -0.27 \pm 0.07$  (sd) from 145 cluster giants and turnoff stars, only slightly higher than  $[Fe/H] = -0.32 \pm 0.03$  (sem) from 257 stars near the turnoff (Anthony-Twarog et al. 2016).

While individual [Ca/H], [Ni/H], and [Si/H] values, based on one to three lines for each star, are presented in Table 4, a more robust view is again supplied by median values for the 24 -29 stars with successful line measurements. From 24 stars, the median  $[Ca/H] = -0.48 \pm 0.19$ , where the quoted error indicates the MAD statistic; from 29 stars, [Ni/H] =  $-0.61 \pm 0.06$ ; and from 28 stars, median [Si/H] =  $-0.44 \pm 0.11$ . Relative to the adopted cluster [Fe/H] = -0.55, these values represent [A/Fe] values of 0.07, -0.06, and 0.10 for Ca, Ni, and Si, respectively, consistent within the uncertainties with little to no differential elemental enhancement in the cluster.

Table 5 summarizes the input atmospheric parameters and spectroscopic results for each likely member star with a Hydra spectrum, with the exceptions of W2135, W1133, and W716 for reasons summarized above. Figure 3 illustrates the run of [Fe/H] values as a function of  $T_{\rm eff}$  for which significant sensitivity might be a concern, and as a function of S/N for our sample. No significant trends are discernible here, as was also the case for [Fe/H] with respect to  $\log g$  or  $\xi$ .

### 3.3. Hydra Spectroscopic Uncertainties and Comparisons with Other Spectroscopic Work

Probing the effects of incremented/decremented atmospheric parameters was particularly rewarding in the analysis of NGC 6819 Hydra spectroscopy by Lee-Brown et al. (2015) owing to the large number of stars and the thoroughly populated CMD distribution, with an extensive error propagation map presented in Figure 5 of that paper. We probed a subset of our smaller sample to verify that similar trends are found in NGC 2243. Four stars in different parts of the CMD were reanalyzed with incremented/decremented atmospheric parameters to probe the sensitivity of [Fe/H] estimates to incorrect parameter choices, resulting in similar effects. Although the results are not necessarily symmetric for increments/decrements in relevant quantities, we will conform to the convention presented in Lee-Brown et al. (2015) and summarize the consequences of adopted  $T_{\rm eff}$  values too high by 100 K, surface gravities too small by 0.25, and microturbulent velocities too high by 0.25 km s<sup>-1</sup>.

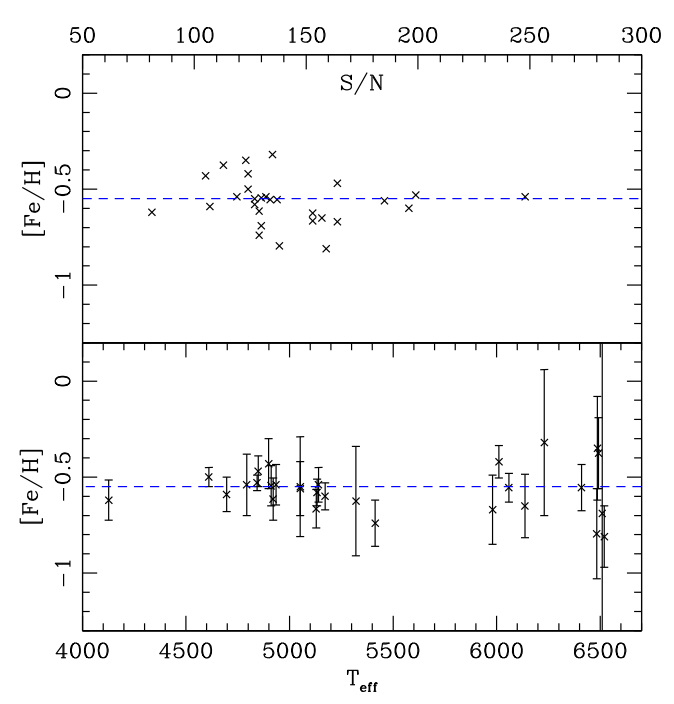
For cooler stars, assignment of a  $T_{\rm eff}$  too high by 100 K results in a derived [Fe/H] too high by 0.08 dex, with a marginally smaller effect (+0.07) for stars near the turnoff. It should be noted that a  $\Delta T_{\rm eff}$  this large would imply a B-V color or reddening error of 0.06 mag for cooler giants or 0.02 mag for stars nearer the turnoff. The abundance effect of log g values assumed to be too small by 0.25 is only discernible for cooler giants, amounting to  $\Delta [{\rm Fe/H}] = -0.02$ , (i.e., lower

 Table 5

 Individual Abundance Information for NGC 2243 Stars, Hydra Sample

W ID	$T_{ m eff}$	log g	ξ	[Fe/H]	MAD	Num.	[Ca/H]	[Ni/H]	[Si/H]
519	6199	3.75	1.72	-0.62	0.17	10	-0.65	-0.65	
611	5052	3.25	1.34	-0.56	0.14	17	-0.40	-0.55	-0.35
873	6055	3.75	1.61	-0.62	0.19	11	-0.46	-0.55	-0.47
1044	6337	3.80	1.82	-0.26	0.37	10	-0.74	-0.62	-0.55
1230	5321	3.60	1.28	-0.67	0.24	11	-0.42	-0.74	-0.39
1263	5172	3.20	1.38	-0.60	0.07	15	-0.43	-0.63	-0.71
1266	6089	3.75	1.64	-0.37	0.10	10	-0.57	-0.41	-0.21
1271	4935	2.50	1.50	-0.55	0.12	15	-0.31	-0.60	-0.40
1294	5052	3.25	1.34	-0.55	0.26	17	-0.48	-0.66	-0.53
1313	4610	2.00	1.60	-0.50	0.05	15	•••	-0.53	-0.34
1421	5129	3.40	1.30	-0.66	0.10	14	-0.66	-0.72	-0.12
1436	6396	3.85	1.85	-0.57	0.12	8	-0.92	-0.77	-0.66
1467	4911	2.50	1.50	-0.52	0.11	15	-0.21	-0.49	-0.67
1696	4843	2.65	1.47	-0.53	0.04	16	-0.28	-0.56	-0.35
1738	4921	2.50	1.50	-0.66	0.15	15	-0.12	-0.51	-0.40
1847	4849	2.65	1.47	-0.47	0.08	16	-0.25	-0.61	-0.25
1871	6387	3.85	1.84	-0.89	0.15	5	-0.70	-0.83	-0.55
1995	5133	3.40	1.30	-0.58	0.07	14	-0.37	-0.61	-0.29
2003	6446	3.85	1.90	-0.82	0.23	4	-0.83	-0.78	-0.96
2098	5414	3.60	1.31	-0.74	0.12	13	-0.59	-0.76	-0.44
2394	6128	3.75	1.67	-0.51	0.06	6	-0.65	-0.56	-0.49
2410	4899	2.50	1.50	-0.43	0.12	16	-0.09	-0.47	-0.45
2434	5140	2.60	1.48	-0.54	0.09	17	-0.24	-0.55	-0.33
2676	6506	3.95	1.92	-0.33	0.28	8	-0.73	-0.71	-0.18
2696	6529	3.95	1.94	-0.68	NA	1	-0.77	-0.62	-0.50
2908	6510	3.95	1.92	-0.36	0.19	8	-0.66	-0.60	-0.87
3618	4696	2.35	1.53	-0.60	0.10	16	•••	-0.74	-0.56
3633	4127	1.20	1.76	-0.64	0.07	15	•••	-0.71	-0.80
3728	4793	2.25	1.55	-0.57	0.15	16	•••	-0.55	-0.31

Note. No EW analysis for W2135 was carried out; corresponding atmospheric model parameters would be 4652 K, 2.35, and 1.53 km s<sup>-1</sup>.



**Figure 3.** [Fe/H] as a function of  $T_{\text{eff}}$  and S/N.

log g leads to lower abundance), again similar to results from Lee-Brown et al. (2015). Using microturbulent velocities too small by  $0.25 \text{ km s}^{-1}$  will produce a higher [Fe/H], although

the effects are more  $T_{\rm eff}$  dependent, smallest for turnoff stars (+0.02) to  $\Delta {\rm [Fe/H]} = +0.07$  dex for the cooler giants.

As noted earlier, NGC 2243's place as one of the most metal-poor open clusters is fairly clear despite a historic range of [Fe/H] estimates that is distressingly large. This history is summarized well by recent studies, including Jacobson et al. (2011) and Kovalev et al. (2019). It appears that differences between one study and another cannot always be simply explained as being due to different  $T_{\rm eff}$  scales, although temperature is likely to have the dominant effect on [Fe/H] determination. One of the lower estimates, [Fe/H] = -0.63, was derived by Houdashelt et al. (1992), who employed JHK photometry to derive  $T_{\rm eff}$ . From four stars in common between our analysis set and theirs, we estimate that our  $T_{\rm eff}$  values are hotter by  $109 \pm 69$  K, which alone would account for our 0.08 dex higher estimate of [Fe/H].

With respect to the parametric precepts of Jacobson et al. (2011), we adopt  $T_{\rm eff}$  only 35 K warmer and  $\log g$  values 0.3 dex lower. For giant stars, we would therefore expect these differences to generate approximately offsetting increments to the metallicity, yet the cluster metallicity from Jacobson et al. (2011) using Hydra spectra of higher resolution but lower S/N is  $[{\rm Fe/H}] = -0.42$ , higher than our estimate by more than 0.10 dex.

Magrini et al. (2017) provide detailed  $T_{\rm eff}$ , log g, and  $\xi$  estimates for 13 cool stars in common with the present study, with a resulting cluster average [Fe/H] of -0.35,  $\sim 0.2$  dex higher than our estimate. Based on BV photometry, we would assign  $T_{\rm eff}$  60 K cooler, log g values 0.1 dex smaller, and  $\xi$ 

values  $0.13 \text{ km s}^{-1}$  larger, which would work in the same sense to lower the Magrini et al. (2017) [Fe/H] estimate by no more than 0.07 dex, placing it in the [Fe/H] = -0.4 to -0.5 range.

Sufficient BV photometry exists for stars studied by FR13 to estimate atmospheric parameters for their sample stars in a manner consistent with precepts followed in this study. As noted by FR13, their temperature scale is relatively hot. Differences between their adopted  $T_{\rm eff}$  and values assigned by color—temperature relations from BV photometry range from 150 K for stars below the clump to 250 K or higher for stars near the turnoff. Despite a prediction that lowering their temperature scale would result in lower [Fe/H] and [Li/H] values by  $\geqslant 0.15$  dex, FR13 derive [Fe/H] = -0.54, virtually identical to the median value derived from EW measures in the current study.

Accounting for differences between spectroscopic analyses may require looking beyond the most traceable effects (e.g., differing temperature scales) to causes more difficult to probe. These may include atmospheric models, line lists, and adopted log *gf* values in addition to operational differences, e.g., continuum level estimation and line measurement techniques. Alternatively, it may be useful to consider methods that train and utilize neural networks to analyze spectra in a holistic manner.

We previously developed and used such a neural network classification approach called ANNA (Lee-Brown et al. 2015; Lee-Brown 2017, 2018) in similar contexts, especially NGC 2506 and NGC 6819 (Anthony-Twarog et al. 2018; Deliyannis et al. 2019). Data from NGC 2506 successfully analyzed using ANNA were obtained in the course of the same runs as our Hydra spectra in NGC 2243, so the same training parameters developed could be applied to NGC 2243 Hydra spectra. This application is not obviously straightforward because the ANNA training set was developed using Kurucz atmospheric models more metal-rich than [Fe/H] = -0.50, making extrapolation to lower [Fe/H] unreliable. We restrict our reference to ANNA results for the cooler, evolved stars in NGC 2243, for which the median [Fe/H] value for 16 stars is  $-0.42 \pm 0.03$ , keeping in mind that this value is a likely upper limit to the true cluster metallicity.

Kovalev et al. (2019) have also developed a neural network approach to parameter estimation, using both LTE and non-LTE (NLTE) atmospheric models. As with ANNA, "the Payne" code first trains on a large set of synthesized spectra and then performs fits. With a training set built on atmospheric models that include considerably lower [Fe/H] values than ANNA, "the Payne" is well situated to provide parameter estimates for globular clusters and open clusters, as described in Kovalev et al. (2019), where NGC 2243 and a more metalrich open cluster, NGC 3532, are discussed. A total of 82 likely members of NGC 2243 were selected using radial velocity and Gaia proper-motion criteria. An intracluster spread of 0.07 dex in [Fe/H] is estimated for NGC 2243. From the limited specific data provided for NGC 2243 stars, it appears that their derived  $T_{\rm eff}$  for a turnoff star is approximately 150 K hotter than our BV photometry-based values. The LTE result from Kovalev et al. (2019), probably the most appropriate comparison to our LTEbased results, is  $[Fe/H] = -0.57 \pm 0.11$ , where the quoted error refers to a mean systematic error; the NLTE estimate is 0.05 dex higher.

Possible  $\alpha$ -element enhancement in NGC 2243 has been a topic of interest owing to its location in the outer disk of the

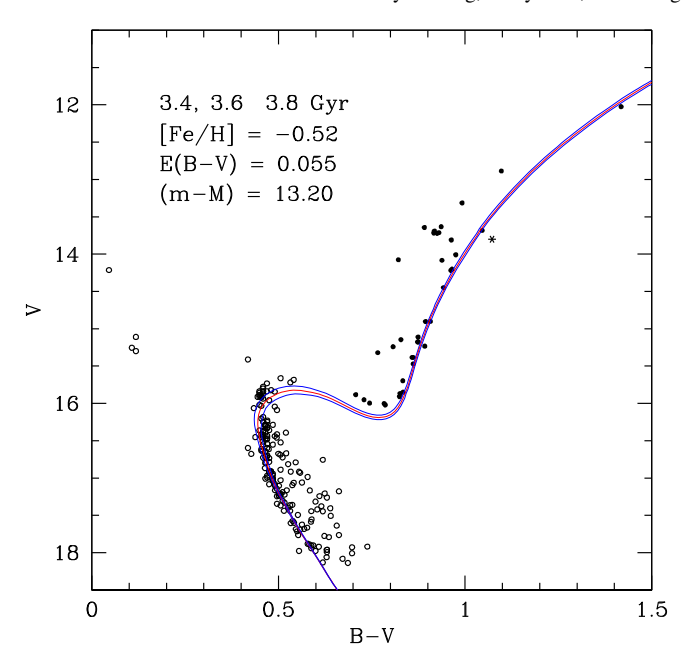


**Figure 4.** CMD comparison to the isochrones of VandenBerg et al. (2006). Isochrones have ages of 3.4, 3.6, and 3.8 Gyr. Filled circles include all cluster members with B-V>0.7. Open circles are highly probable members from the cluster core with CCD B-V photometry, while an asterisk notes the location of W2135.

Milky Way. Gratton & Contarini (1994) analyzed two giants to arrive at [Fe/H] of  $=-0.48\pm0.15$  for the cluster, paying additional attention to a variety of other elements, including  $\alpha$ -elements, concluding that a scaled-solar abundance pattern was neither excluded nor strongly favored, with typical enhancements  $[\alpha/Fe]$  of 0.07. More recently, Jacobson et al. (2011) find elemental enhancements  $[X/Fe] \leq 0.15$ , consistent with scaled-solar abundances. In particular, they cite strong evidence of solar [O/Fe] for one of the giants in NGC 2243.

Similarly, Kovalev et al. (2019) cite only modest evidence for  $\alpha$ -element enhancement,  $+0.20 \pm 0.22$  for [Ti/Fe], while FR13 again find [Fe/H] =  $-0.54 \pm 0.10$ , with modest or null indications of enhancement for Ca or Si.

#### 4. The CMD: Cluster Age and Distance

To place the stellar population within NGC 2243 and the cluster itself in the appropriate context for evaluation and interpretation of the Li patterns described below, we show in Figure 4 the CMD of well-defined cluster members relative to an appropriate set of VR isochrones. The filled circles include all member cluster giants with B - V > 0.70; the open circles are core cluster members with Gaia probabilities ≥0.7 and CCD BV photometry, while the asterisk again notes W2135. The compilation of the BV photometry is described in Section 2.4. The adopted isochrones have [Fe/H] = -0.52and are scaled-solar models. While slightly higher than the spectroscopically derived range of [Fe/H] = -0.53 to -0.56(Section 3.2), the minor offset of the isochrones can account, in part, for the possibility of a minor  $\alpha$ -element enhancement. For consistency with the standard adopted in our previous cluster analyses using VR isochrones, we first zero the isochrones by requiring that a star of solar mass and metallicity at an age of 4.6 Gyr have  $M_V = 4.84$  and B - V = 0.65, leading to minor adjustments,  $\Delta V = 0.02$  and  $\Delta (B - V) = +0.013$  mag. The assumed cluster reddening is E(B-V) = 0.055 (Section 2.5).

The isochrones have been shifted by an apparent distance modulus of 13.20 and have ages of 3.4, 3.6, and 3.8 Gyr.

The average parallaxes for the stars plotted in Figure 4 yield an apparent modulus of (m-M)=13.55 with an appropriate contribution from the adopted reddening. However, this does not account for the often-discussed likelihood of a zero-point offset of  $-0.05\pm0.03$  mas in the Gaia parallaxes, especially for stars at greater distance (see, e.g., Cantat-Gaudin et al. 2018; Riess et al. 2018; Stassun & Torres 2018; Zinn et al. 2019). Applying a typical correction of +0.05 mas to the cluster Gaia DR2 parallax generates (m-M)=13.1, clearly in much better agreement with the isochrone fit.

While the isochronal giant branches are an excellent match to the observational trends, the colors of the turnoff stars extend across the full color range of the isochrones, showing more structure than implied by the models. The luminosities of the subgiant stars also appear to lie above the isochrones, which might reflect an age on the lower side of our proposed range. As a compromise, we will adopt  $3.6 \pm 0.2$  Gyr as the cluster age and use that isochrone to transfer from the observational to the theoretical plane and to delineate the stellar masses for the stars within our Li sample.

#### 5. Lithium Abundances and Trends

#### 5.1. Spectrum Synthesis and Data Merger

We have utilized spectrum synthesis techniques to estimate A(Li) for all high-S/N spectra in our Hydra sample, augmented by available archive spectra from the VLT; these stars have summarized in Tables 1 and 2, respectively. For this purpose, we used the synth mode of MOOG (Sneden 1973), referencing the spectra to model atmospheres appropriate to each star. As described in Section 3.2,  $T_{\rm eff}$  are derived in an internally consistent manner from homogeneous B - V colors using two color-temperature relations adopted in previous investigations by this group. Interactive estimation of A(Li) in the synthesis process also provides an opportunity to verify that the adopted  $T_{\rm eff}$  for each star is appropriate, based on simultaneous agreement of the several temperature-dependent lines near 6710 Å. Table 6 summarizes the results of synthesis on all spectra, with consensus A(Li) estimates that summarize results from Hydra, Giraffe, and UVES spectra. S/N values for the Hydra and VLT samples may be found in Tables 1 and 2. While a standard for S/N values generally  $\ge 100$  is desirable, a few exceptions were made for VLT spectra to deliberately expand the very small overlap with the previous Li abundance samples of FR13 and HP. Adopted atmospheric model parameters are found in Tables 5 and 2 for the two spectroscopic samples. The consensus or overall A(Li) value was arrived at with the following general considerations: spectra with higher S/N were favored, with higher resolution dominating only if S/N values are comparable. All other factors being comparable, results from our own Hydra spectra were favored. Of 14 Hydra stars for which VLT spectra were also available, 13 fell within the same category for both sources, i.e., classed as detections or upper limits in both cases. Only W3618 was switched from an upper limit of A(Li) = 0.65using Hydra spectra to a detection of A(Li) = 0.65 from VLT.

Comparison of these Li abundances with prior work is complicated by differences of methodology and temperature scales, with the expectation that the latter would provide the dominant influence. FR13 make primary use of VI photometry

**Table 6** A(Li) Derived from Synthesis

ID	Adopted	Hydra		Gira	ıffe	UVES	
ID.	A(Li)	A(Li)	EW	A(Li)	EW	A(Li)	EWª
239	≤0.6			€0.6	7	€0.7	1.8
365	0.75	•••		•••		0.75	16
519	2.9	2.9	82.2	•••			
611	1.1	1.1	31.5	1.0	26		
873	2.45	2.45	44.2	•••			
910	≤0.1	•••		≤0.6	12.8	≤0.1	3.1
1044	2.6	2.6	39	•••			
1230	≤1.1	≤1.1	7	•••			
1261	1.2	•••		1.2	16	•••	
1263	≤1.1	≤1.1	13	≤1.0	12		
1266	2.4	2.4	49.4	2.4	42.3	•••	
1271	≤0.6	≤0.6	10.5	≤0.6	15	≤0.4	3.5
1294	≤0.5	≤0.5	7.9	≤0.8	5	•••	
1313	≤0.0	≤0	13.5			≤-0.2	2.6
1421	≤0.6	≤0.6	4.2			•••	
1436	2.4	2.4	19				
1467	≤0.1	≤0.1	11.5	≤0.6	20.6	≤0.2	5
1679	≤1.2			≤1.2	9		
1686	2.85	•••		2.85	49	•••	
1696	≤0.6	≤0.6	11.6			≤0.6	16
1738	≤0.3	≤0.3	8.8				
1847	0.75	0.75	26.7			0.95	16
1871	2.3	2.3	20.4			•••	
1923	€2.1	•••		≤2.1	3.3	•••	
1995	≤0.8	≤0.8	7.8			•••	
2003	2.6	2.6	33.4	•••			
2098	≤1.4	≤1.4	7.2	•••		•••	
2135	1.0	1.0	42.6	1.0	43	1.05	78
2195	€1.2	•••		≤1.2	5		
2394	3.1	3.1	112	•••		•••	
2410	≤0.3	≤0.5	17.3	•••		≤0.3	4.5
2434	≤0.7	≤0.7	11.2	•••		•••	
2536	≤0.7	•••		≤0.7	9	•••	
2613	1.25	•••		1.25	28	•••	
2648	1.15	•••		•••		1.15	39
2676	2.0	2.0	17.2	•••			
2696	2.4	2.4	22.4	•••		•••	
2908	2.1	2.1	17	•••			
3618	0.65	≤0.65	33.3	•••		0.65	15
3633	≤−0.9	≤-0.9	33.9	•••		$\leq -0.4$	12
3728	≤0.4	≤0.4	15.2	≤0.0	14.5	≤0.1	4.7

#### Note

from Kaluzny et al. (1996), coupled with their fairly high reddening correction, equivalent to almost E (B-V) = 0.08. FR13 note in their paper that a prior study by HP employs a lower reddening value with consequently lower temperatures. Figure 6 of FR13 illustrates both samples in a magnitude— $T_{\rm eff}$  plane with a substantial temperature offset between the two samples amounting to 200 K and resulting in Li abundances lower by 0.15 dex in HP.

Figure 1 illustrated our sample (filled black points), as well as those analyzed by FR13 (blue points) and HP (red points); the photometry is the BV photometry described in Section 2.5. Clearly no intrinsic  $T_{\rm eff}$  offset, as defined by B-V, between the samples is evident. It remains important, therefore, to

<sup>&</sup>lt;sup>a</sup> Measured EWs for UVES spectra refer only to Li line at 6707.78 Å. EWs listed for HYDRA and Giraffe spectra include a contribution from the nearby Fe line.

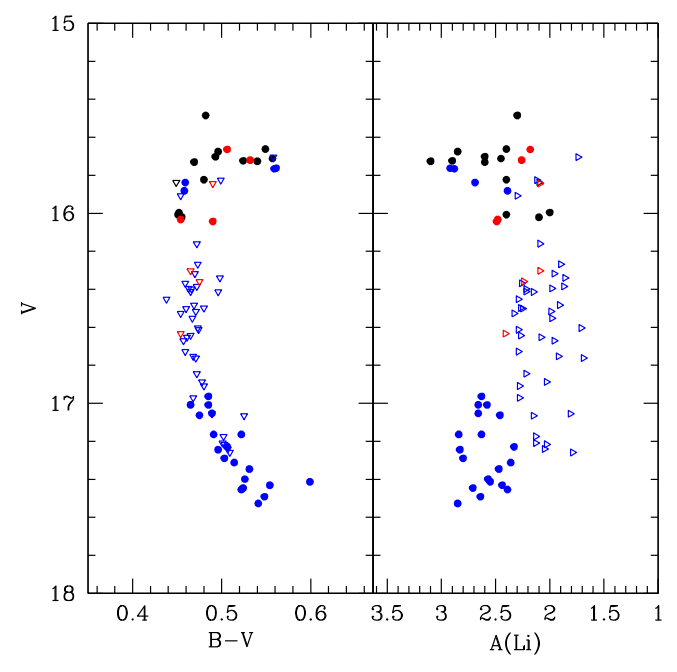


**Figure 5.** A(Li) estimates for stars at the CMD turnoff. Symbol colors have the same meaning as in Figure 1. Filled circles are Li detections, while triangles denote upper limits to A(Li).

investigate the  $T_{\rm eff}$  differentials before discussing all available Li abundances in a homogenous manner.

Having found or synthesized colors for all of HP's and FR13's sample, we estimated  $T_{\rm eff}$  values for all stars based on color-temperature relations discussed above. FR13's use of a higher reddening value than used in the present study implies  $T_{\rm eff}$  for near-turnoff stars that are  $\geq 250 \,\mathrm{K}$  higher in their analysis, while cooler giants are taken to be  $\geq 150$  K hotter than our assessment would be. FR13 themselves estimate that temperatures higher by 200 K imply A(Li) values higher by 0.15 dex. We sought to validate this estimate in two ways. First, there are a handful of stars with abundances based on our synthesis analysis that overlap with the FR13 sample, none of them from our original Hydra sample but from the augmented archival VLT spectra. Three stars from Table 2 with detections overlap with FR13 detections, W1261, W1686, and W2648. In the case of W1686, our analysis provides A(Li) that is 0.24 dex higher than FR13; conversely, our analysis yields an Li abundance for W2648 that is 0.36 lower. Our estimated A(Li) for W1261 is only 0.04 dex smaller than that of FR13. No direct overlap of samples between the results presented in Tables 1 and 2 and those of HP exists at all.

Another way to estimate the effect of increments in  $T_{\rm eff}$  is to repeat the synthesis analysis on our available spectra using models with higher temperatures. Test cases suggest that use of models with temperatures higher by 200 K for cooler stars and 300 K for turnoff stars would produce Li abundances values higher by 0.2 dex. It is unclear whether other differences in methodology (continuum placement, use of EWs, a higher assumed overall metallicity) between our results and those from other surveys mask or negate some of this offset. Since the direct comparison of our A(Li) values for two stars in common with FR13 is indeterminate, we elect to present Li abundances from FR13 and HP with no adjustment in the following discussion.

#### 5.2. Li Trends: The Turnoff Region

Figure 5 illustrates the run of A(Li) values with respect to V magnitude and B - V color for all samples, with inverted triangles noting the location of upper limit values. A number of features are immediately apparent. First, in the CMD region where the FR13 data, the stars of Tables 1 and 2, and the A(Li) results of HP overlap, i.e., at the top of the turnoff with V < 16.0, the FR13 sample (blue points) does not separate toward a higher A(Li) from the current sample (black points) or HP (red points), as one might expect given the higher temperature scale used by FR13. The largest detected Li abundance in the FR13 analysis is A(Li) = 2.9, 0.2 dex lower than the highest abundance derived for our sample. The probability of attaining a higher limiting A(Li) is undoubtedly enhanced by a sample of 12 stars from the current study relative to four from FR13, one of the reasons for boosting the population of stars observed within this critical evolutionary phase. Second, in contrast, the generally fainter stars explored in great depth by FR13 map out the Li dip extraordinarily well, particularly at the faint end. Near V = 16, the addition of five members from the current study and HP illustrates the strikingly steep high-mass/bright edge of the Li dip, hereinafter referred to as the wall. This feature emerges in all wellpopulated cluster samples older than the Hyades (Twarog et al. 2020) where stars entering the subgiant branch have masses outside the range of the Li dip. The addition of these stars shifts the start of the Li dip approximately 0.2 mag fainter than allowed from the FR13 data alone. Whether the limit could be pushed another 0.1 mag fainter still requires an even more expanded sample and cannot be answered at present. Third, the cool edge of the Li dip where measurable detections of Li, rather than upper limits, recur is starkly apparent near V = 16.95. While one could argue that the spread in A(Li) at this magnitude level runs from the upper limit above the Li dip to the lowest measured value within the Li dip, FR13 has emphasized that the stars below V = 16.95 with only detection limits are the likely product of spectra with low S/N and unlikely to be indicative of the true Li abundance among the fainter stars. Unfortunately, FR13 do not supply S/N data for individual stars, so the role of this parameter in setting the scatter among the fainter dwarfs remains ambiguous. Fourth, among the stars above the Li dip (V < 16.05), A(Li) covers the range from  $\sim$ 3.1 to an upper limit near 1.75. Unlike the scatter in A(Li) at the faint end, the S/N of the spectra among the majority of stars in this CMD region is high enough that the scatter is reflective of a real scatter in abundance. We will return to this key observation when discussing evolution from the main sequence through the giant branch in the following section.

Using the isochrones of Figure 4 and an age of 3.6 Gyr, we can translate the Li trend with V at the turnoff into Li versus mass, as shown in Figure 6. Stars from the subgiant branch beyond B-V=0.7 and all red giants have been excluded from the plot because the mass range among these stars is too small to allow differentiation on this scale. Taking the discrete nature of the mass estimates into account and reiterating the greater uncertainty in the Li estimates at the lower-mass end of the distribution, a plausible mass range encompassing the Li dip for NGC 2243 runs from  $1.09 \pm 0.015\,M_{\odot}$  to  $1.21 \pm 0.01\,M_{\odot}$ , for a center at  $1.15 \pm 0.018\,M_{\odot}$ . As discussed in D19, defining the optimal position for intercomparison of the Li dips among multiple clusters can be a challenge. Clusters such as NGC

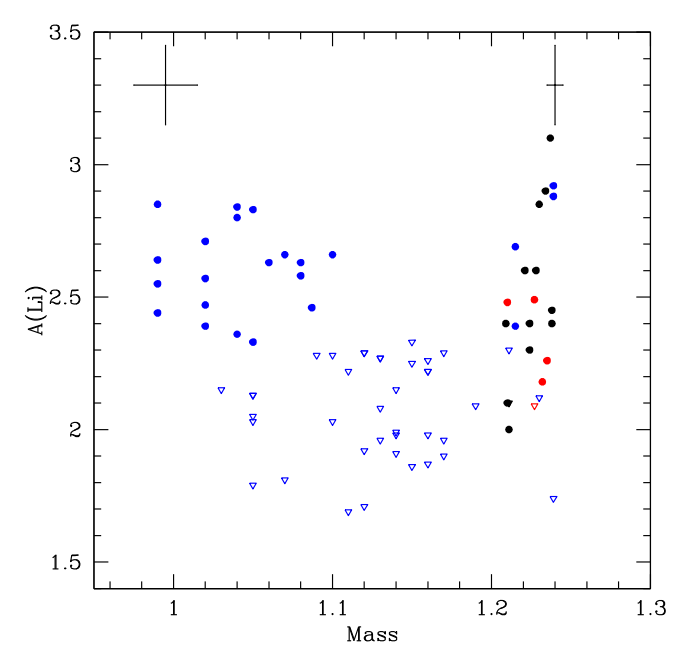


**Figure 6.** Mass map of the stars populating the region of the Li dip as shown in Figure 5. Symbols have the same meaning as in Figure 5. Masses are derived from a VR isochrone of 3.6 Gyr age as delineated in Figure 4. Crosses illustrate the typical error bars for A(Li) and mass at the extreme ends of the mass scale.

3680 and NGC 752 are inadequately populated and/or spectroscopically sampled to provide definitive boundaries for the edges of the Li dip, though attempts have been made to approximate the location of the center of the composite cluster sample to estimate the trend with central mass with varying [Fe/H]. Anthony-Twarog et al. (2009), assuming a symmetric Li dip and comparing the composite cluster sample with the well-defined Hyades distribution, derived a linear mass relation of  $M_{\text{center}}/M_{\odot} = 0.4^*[\text{Fe/H}] + 1.38$ . With [Fe/H] = -0.04 and a much richer sample to outline the boundaries of the Li dip, D19 found excellent agreement between this relation and NGC 6819. If we extrapolate to [Fe/H] = -0.55, the center of the Li dip in NGC 2243 should sit at  $1.16 \, M_{\odot}$ , clearly consistent with the observations.

It should be emphasized that attempts have been made to use alternate markers to test the impact of metallicity on the evolution of the Li dip, most notably the cool boundary of the feature (see, e.g., Cummings et al. 2012; FR13). The clear benefit in this approach is the survival of the lower-mass boundary to a much greater age, allowing extension of the possible trend with [Fe/H] to a wider array of clusters with a greater range in metallicity, if precision spectroscopy can be obtained at the fainter luminosities of these stars. The greater age of a cluster also has an important drawback: A(Li) for stars lower in mass than the Li dip does not remain fixed with time. A(Li) for stars at lower mass rises out of the Li dip before plateauing and declining with decreasing mass. The rise to, and the level of, the Li plateau changes with age, making the exact definition of the boundary of the Li dip increasingly indeterminate.

While it does have applicability to a limited range of cluster ages, with a range that depends on [Fe/H], the A(Li) wall at the high-mass boundary is usually readily identifiable if a sufficient sampling of the mass range can be accomplished. With the addition of NGC 2243, we can extend the mass boundary from the rich, well-sampled Hyades cluster at [Fe/H] = +0.15

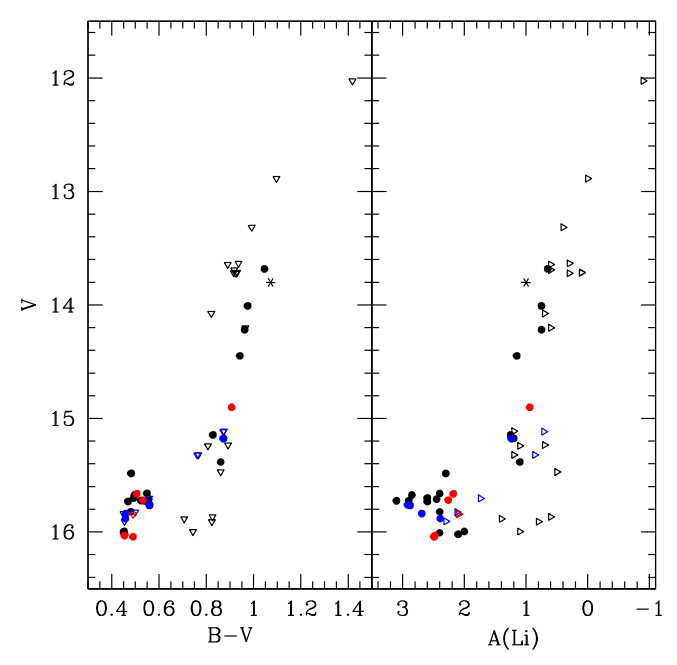


**Figure 7.** A(Li) for stars from the top of the turnoff through the giant branch as a function of *V*. Symbols have the same meaning as in Figure 5.

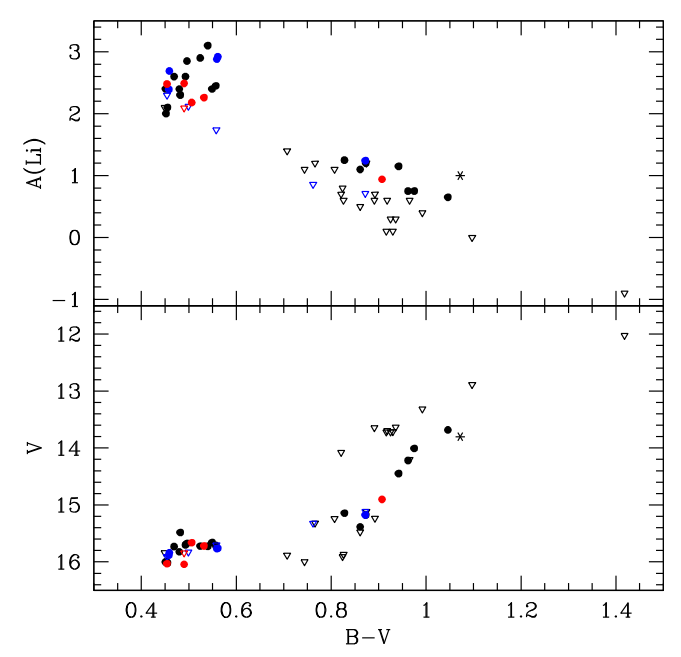


**Figure 8.** A(Li) for stars from the top of the turnoff through the giant branch as a function of B - V. Symbols have the same meaning as in Figure 5, with an asterisk noting the position of W2135.

(Anthony-Twarog et al. 2009; Cummings et al. 2017) and  $1.494\,M_\odot$  to NGC 6819 at [Fe/H] = -0.04 and  $1.43\,M_\odot$  to NGC 2243 at [Fe/H] = -0.55 and  $1.21\,M_\odot$ . A simple linear fit through these data generates  $M_{\rm wall}/M_\odot = 0.41^* [{\rm Fe/H}] + 1.44$ . We will return to this well-documented decline in mass with decreasing [Fe/H] in Section 6.

# 5.3. Li Trends: Post-main-sequence Evolution

Figures 7 and 8 illustrate the trends of A(Li) for stars leaving the main sequence and evolving across the subgiant branch, up the giant branch, and eventually to the red giant clump.

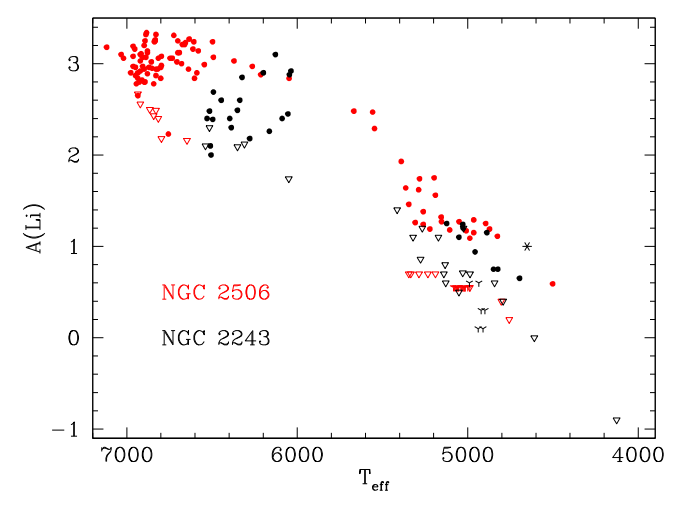


**Figure 9.** Contrast of the A(Li) distribution with  $T_{\rm eff}$  for stars more massive than the Li dip in NGC 2506 (red) and NGC 2243 (black). Filled symbols are detections; open triangles and three-point stars are upper limits, with the latter tagging clump stars. An asterisk notes the location of W2135.

Figure 7 separates the data by V magnitude, while Figure 8 details the trends with color. The turnoff region for each plot includes only stars at masses that place them outside the Li dip. Keeping in mind the typically high S/N for the spectra at the top of the turnoff, it must be concluded that the order-of-magnitude spread in A(Li) among stars with Li detections at the top of the turnoff is real. Equally important, the range in A(Li) is not correlated with position in the CMD, either in color or in luminosity.

By the time these stars evolve to the base of the giant branch, A(Li) is further reduced to a degree that places all the stars at or below the canonical Li-rich boundary of A(Li) = 1.5 (Kumar et al. 2020). Continuing up the giant branch, there is a general decline in A(Li) for stars with detectable Li; above the level of the red giant clump and within the clump itself, no star has detectable Li, with the upper limits set at A(Li) = 0.7 or lower.

# 5.4. Li Patterns: The Role of NGC 2243

In the same way that NGC 2243 extends and strengthens the pattern of declining mass boundaries for the Li dip with decreasing [Fe/H], its combination of low [Fe/H] and significant age places it in a unique position for testing the evolutionary trends for stars more massive than the Li dip, while on the main sequence and beyond. Using the Hyades-Praesepe ([Fe/H] = +0.15, age = 0.65 Gyr) as a zero-point and a mix of clusters ranging in age from 1.5 Gyr (NGC 7789) to 2.25 Gyr (NGC 6819) and [Fe/H] as low as -0.3 (NGC 2506), D19 lay out a detailed interpretation of the manner and degree to which stars above the Li wall alter their surface A(Li) prior to leaving the main sequence and crossing the subgiant branch, where the traditionally expected impacts of a deepening convective zone and potential internal mixing dominate. In summary, it was noted that, contrary to expectation, the range in A(Li) among the stars above the wall expanded downward from the probable primordial cluster value with increasing cluster age.

For the first test of this trend, we show in Figure 9 a comparison of the variation of A(Li) for all stars above the Li dip from the turnoff through the giant branch for NGC 2243 (black) and NGC 2506 (red). Stars with only upper limits to the Li abundance are shown as triangles; stars with upper limits

within the respective red giant clumps are three-point crosses. Being the closest in metallicity to NGC 2243 ([Fe/H] = -0.55), NGC 2506 (-0.3) should approximate the Li appearance of NGC 2243 at a younger age (1.85 Gyr vs. 3.6 Gyr), keeping in mind that the differential "Li age" is smaller owing to the higher-mass boundaries of the Li dip for a more metal-rich cluster. Note also that the  $T_{\rm eff}$  scale of the turnoff stars in NGC 2506 is hotter than that of NGC 2243 owing to the younger isochronal age of the cluster.

Two striking features emerge from a comparison of the two distributions. First, among the turnoff stars in NGC 2506, 85% have A(Li) within 0.6 dex of the maximum cluster value at the turnoff; the remaining 15% outside this range include both detections and upper limits. By contrast, keeping in mind the sparser sample from the turnoff of NGC 2243, there is an almost uniform distribution of stars extending from the upper bound in A(Li) to 1.1 dex lower. For the older cluster, more than 2/3 of the turnoff stars lie below the 0.6 dex boundary in A(Li). Second, the turnoff distinction translates directly to the giant branch distribution. As discussed in Anthony-Twarog et al. (2018), despite its moderately young age, the subgiant branch in NGC 2506 is sufficiently populated to allow delineation of the depletion of Li as stars evolve from a typical turnoff value near A(Li)  $\sim$ 3.0 to a detection value of  $\sim$ 1.4 near the base of the giant branch. By contrast, the typical value for stars leaving the main sequence in NGC 2243 is ~2.5, and all stars at the base of the giant branch have only upper limits of A(Li)  $\sim$ 1.2. This is clearly not the complete story since 10 stars with Li detections in NGC 2243 do overlap nicely with the giant detections within NGC 2506. Ignoring red clump stars, all of which are upper limits only in both clusters, the implication is as follows: the dominant range in A(Li) among stars leaving the main sequence in NGC 2243 is typically twice as large as that within NGC 2506 (1.1 dex vs. 0.5 dex). Depletion across the subgiant branch reduces the typical abundance at the base of the giant branch to A(Li) = 1.2 or higher for NGC 2506, leaving these stars above the detection limits of the spectroscopy. Stars that fall within the 15% sample at the lower end of the main-sequence A(Li) distribution are depleted to a comparable extent, placing them as only upper limits near the giant base, accounting for the handful of nondetections near 5300 K. For NGC 2243, clump stars aside, the ratio of nondetections to detections is 3/2 among the red giants, consistent within the uncertainties with the wide and almost uniform A(Li) distribution range among the turnoff stars. We conclude that the pattern observed among the giants merely reflects a range in extant Li in stars on the point of leaving the main sequence, convolved with one or more depletion mechanisms (e.g., dilution and/or rotationally induced mixing) as the stars evolve along the subgiant branch and the firstascent giant branch.

To get some clarity on the potential source of the differences between NGC 2506 and NGC 2243, we turn to an older and more metal-rich cluster, NGC 6819. While only 0.4 Gyr older than NGC 2506, from the standpoint of "Li age," the cluster is significantly more advanced owing to its higher metallicity ([Fe/H] = -0.04). This positions the Li dip within a mass range 0.1  $M_{\odot}$  higher than in NGC 2506; its turnoff stars (above the Li dip) are in a closer evolutionary state relative to the Li dip to those in NGC 2243 rather than NGC 2506. As a simplistic means of quantifying this evolutionary phase, we note that the range in magnitude for stars above the Li dip in

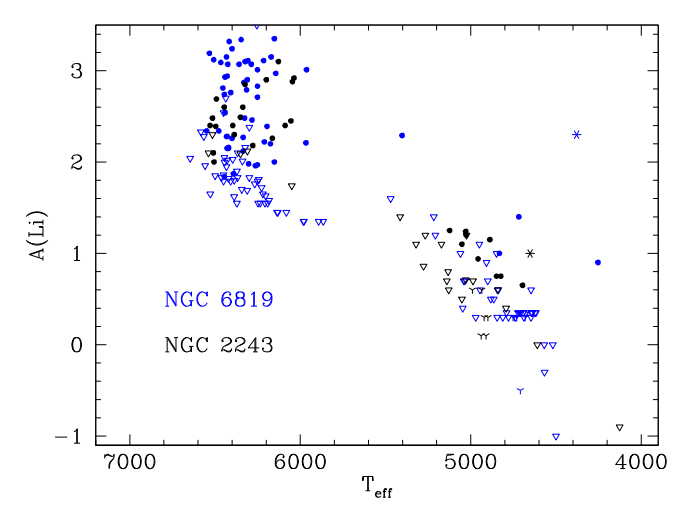


**Figure 10.** Same as Figure 9, but for NGC 6819 (blue) and NGC 2243 (black). Clump stars in NGC 6819 are, like the majority of giants, all upper limits. No distinction is made between first-ascent and clump giants in NGC 6819. Asterisks note the presence of Li-rich giants W2135 in NGC 2243 and W7017 in NGC 6819.

the three clusters of interest is, binaries aside, 0.6, 1.0, and >1.4 mag for NGC 2243, NGC 6819, and NGC 2506, respectively. The lower bound is given for NGC 2506 because the exact location of the wall of the Li dip in this cluster has not yet been determined (Anthony-Twarog et al. 2018). Figure 10 reveals the NGC 6819 analog to Figure 9, with the notable change that no distinction is made between upper limits in A(Li) for clump giants relative to first-ascent giants since so few giants of any category in NGC 6819 exhibit Li detections.

Comparison of Figure 10 with Figure 9 demonstrates that the NGC 6819 turnoff distribution bears a much stronger similarity to NGC 2243 than NGC 2506. Keeping in mind the statistically richer sample of NGC 6819, the range in A(Li) among detections is 1.4 dex; including upper limits, the range extends to 2.0 dex. More relevant, the distribution is even more heavily weighted toward lower A(Li) than in NGC 2243; 30% of the sample lies within 0.6 dex of the cluster limit, but 63% are more than 1 dex below the cluster limit and are dominated by upper limits rather than detections (D19). Because the range in A(Li) among the stars hotter than 5800 K is uncorrelated with either luminosity or  $T_{\rm eff}$  above the Li dip, stars reaching the base of the giant branch should exhibit a comparable spread in A(Li), assuming that the depletion mechanism on the subgiant branch applies equally to all stars independent of their initial A(Li) upon entering the subgiant branch. The ubiquity of upper limits among the giants in NGC 6819 is consistent with this prediction given the turnoff distribution weighted toward depleted Li. Clearly, some stars retain enough Li to fall within the detection limits, supposedly the descendants of the stars leaving the main sequence, with Li relatively unchanged from the primordial cluster value. Only five stars cooler than 5600 K in NGC 6819 have detectable Li. Of the two stars with A(Li) greater than 2.0, one lies on the subgiant branch between the turnoff and the base of the giant branch, while the second is WOCS7017, an Li-rich giant now known to be a clump star of anomalously low mass (Anthony-Twarog et al. 2013; Carlberg et al. 2015; Handberg et al. 2017).

Given Figures 9 and 10, the question remains, which stellar parameter(s) control(s) the turnoff distribution of A(Li) as a function of age and metallicity and thus the trend among the

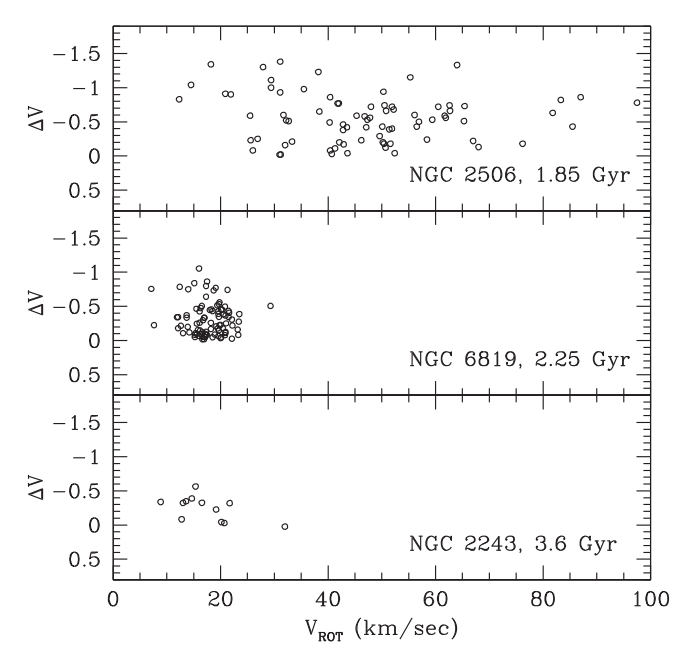


**Figure 11.** Distribution in  $v_{\rm rot}$  for stars above Li dip for NGC 2506, NGC 6819, and NGC 2243. From the standpoint of Li evolution, NGC 6819 and NGC 2243 are of comparable age and much older than NGC 2506, in contrast with the listed isochronal ages.  $\Delta V = 0$  is defined by the wall of the Li dip.

giants? Following the illuminating discussion of D19, we show in Figure 11 the range of  $v_{\rm rot}$  as a function of the star's position above the wall of the Li dip, a more restricted version of their Figure 11, including only the three clusters under discussion, NGC 2243, NGC 6819, and NGC 2506 and plotting only stars outside the Li dip.  $\Delta V$  is the distance in magnitudes a star lies positioned above the wall of the Li dip, in the sense  $(V_{\rm star} - V_{\rm wall})$ . The velocity range within the youngest cluster (from an "Li age" standpoint) is just under 100 km s<sup>-1</sup>; for both NGC 6819 and NGC 2243, the range is virtually identical, with only one star in each cluster above 25 km s<sup>-1</sup>.

When placed in the context of all the clusters detailed in D19, it is concluded that the primary control of the Li distribution with age for stars above the Li wall is the rotational spin-down of stars from an initial range close to or greater than  $100 \, \mathrm{km \, s^{-1}}$  (NGC 7789 and NGC 2506) to less than 25 km s<sup>-1</sup> (NGC 6819 and NGC 2243). The spin-down mechanism, while still on the main sequence, is correlated with and/or triggers the variable decline in Li among stars with a significant range in primordial  $v_{\rm rot}$ , generating a smaller range in  $v_{\rm rot}$  with increasing age, but an increasing range downward in A(Li) from the primordial cluster value.

It should be emphasized that the A(Li) distribution for stars above the wall prior to rotational spin-down on the main sequence need not be a single-valued peak set at the initial cluster value. Diffusion of Li, with the degree of depletion defined by the level of rotational mixing, could produce a range of A(Li) among turnoff stars prior to rotational spin-down, as seen, for example, among the turnoff stars in NGC 2506 in Figure 9. The spin-down would then initially raise the atmospheric Li content as Li from stable layers below the surface is mixed to the surface, supposedly returning the star to its primordial value before enhanced rotational mixing drives the retrieved Li content to even greater depth and destruction. This process could be indicated by the Li trend among the subgiants in Figure 8 between B - V = 0.45 and 0.6, but the

sample remains too small and the data sources too heterogeneous to reach any definitive conclusion.

We have shown that both age and metallicity are important parameters for Li depletion. Two clusters of roughly similar age (NGC 2506 and NGC 6819) but different metallicity show substantially different subgiant and giant Li patterns, with NGC 2506 being the more orderly of the two. But it is also true that among the two metal-poor clusters (NGC 2506 and NGC 2243), the older one (NGC 2243) is less orderly and is more similar to NGC 6819. The older, metal-poor cluster bears more resemblance to the younger, metal-rich cluster than it does to the younger, metal-poor cluster. One straightforward implication of this trend is that, assuming that the degree of post-mainsequence Li depletion is independent of the initial Li abundance upon entering the subgiant branch, the range in A(Li) among giants at a given phase of evolution will depend strongly on the mass and metallicity of the stars leaving the main sequence, i.e., classification of a giant as Li-rich or Lipoor requires boundaries that vary with mass, metallicity, and age (Twarog et al. 2020).

#### 6. NGC 2243: Summary and Galactic Implications

High-dispersion spectra have been obtained of 42 stars within the field of the metal-deficient open cluster NGC 2243. From both astrometry and radial velocities, 32 cluster members have been identified and their spectra analyzed. From 29 likely single stars, the overall cluster [Fe/H] is well defined at  $-0.54 \pm 0.11$ , where the error describes the MAD about the sample median value, leading to internal precision for the cluster [Fe/H] below 0.03 dex. A much more restricted sample of lines for  $\alpha$ -elements produces effectively scaled-solar abundances, though the uncertainties are larger. With the metallicity and previously determined reddening in hand, the cluster age and distance are obtained by comparison to an appropriate set of isochrones, generating an age and apparent distance modulus of  $3.6 \pm 0.2$  Gyr and  $(m - M) = 13.2 \pm 0.1$ , respectively. The former value places the cluster in an age range comparable to that of M67, while the latter parameter is in excellent agreement with the predicted parallax-based calculation from Gaia DR2, after correction for the probable zero-point parallax error for a cluster at the large distance of NGC 2243. Since the primary goal of the investigation is the delineation of the Li abundance among stars within the cluster from the main sequence through the giant branch, as well as placing the cluster within the context of Li evolution among the open cluster population with age and metallicity, the Hydra sample was expanded through the inclusion and analysis of high-S/N, high-resolution cluster spectra from the VLT archive and the addition of Li abundances for members only available from the published data of François et al. (2013) and Hill & Pasquini (2000), boosting the total cluster sample to over 100 stars. The expanded sample has the greatest impact in defining the variation of Li among stars more massive than the Li dip, from the top of the turnoff through the giant branch. The Li dip remains clearly defined; what is accomplished by the doubling of the turnoff stars more massive than the dip, all but one of which are detections rather than upper limits, is the clear indication that the cluster upper limit to A(Li) is at least 2.9, with one star positioned near 3.1. This is quite similar to the peak value of 2.96 measured by Randich et al. (2020) despite a higher overall [Fe/H] estimate of -0.38 from Gaia ESO pipeline analysis (references within Randich et al. 2020).

Randich et al. (2020) also correctly note that upper turnoff stars "may have already undergone some post-MS dilution" to their surface Li abundances, making a detection of the peak A(Li) value stochastically vulnerable to sample size and selection.

Moreover, the spread in A(Li) among stars on the verge of entering the subgiant branch is at least 1.1 dex and could be greater than 1.3 dex. This spread is crucial because it is not dependent on specific position within the turnoff region, i.e., stars occupying virtually identical locations within the CMD differ in their A(Li) by 0.9 dex. This spread translates directly into a large spread among giants ascending the giant branch for the first time. Excluding the post-He-flash members of the red clump, all of which have only upper limits to A(Li), the majority of the red giants exhibit only upper limits below A(Li) = 1.5, the nominal value predicted for stars of solar Li upon arrival at the base of the giant branch. (Note that the limits become more restrictive with increasing luminosity owing to the declining  $T_{\rm eff}$  among brighter giants and should not be interpreted as evidence for declining A(Li) with evolution up the giant branch; only the Li detections can illuminate this pattern.) This trend is consistent with the pattern found in the more metal-rich and numerically richer but younger cluster NGC 6819. The implication is that, due to the shift in the Li dip to lower mass at lower [Fe/H], the evolutionary phase of a cluster with respect to Li evolutionary pattern, the "Li age," requires a more metal-deficient cluster to attain a greater age to approach the same "Li age" as a metal-rich cluster.

Within the discussion of Li evolution among stars, the role of the main-sequence/turnoff stars above the wall has been twofold. First, by evaluating the sensitivity of the wall to changes in mass, metallicity, and age, some insight could be gained into the physical process(es) triggering the depletion of Li among main-sequence stars both within the Li dip and beyond. As discussed in detail in D19 and confirmed with the addition of NGC 2243, a controlling factor in the evolutionary history of Li for any star, whether above the wall, within, or below the Li dip, appears to be the spin-down mechanism of the star. The key, but not necessarily the only, difference among the stars at varying masses on the main sequence is whether the decline in rotation occurs rapidly, e.g., during the pre-main-sequence phase, or more gradually (and/or nonlinearly) during main-sequence evolution. The challenge in identifying such trends comes from the fact that the degree of Li depletion is likely to be correlated with the degree of rotational decline, but what one measures is an instantaneous snapshot of the current rotational speed with no a priori knowledge of the star's initial rate upon arrival at the main sequence, though statistical distributions of the kind shown in Figure 11 (and in Figure 11 of D19) can help constrain the likely degree of change. If correct, the spin-down pattern among the cluster samples and the long-standing decline in the mass location of the Li dip with decreasing [Fe/H] point toward a metallicity dependence in the rotational evolution of the main-sequence stars, through an initial  $v_{rot}$  distribution with mass that depends on [Fe/H] and/or a spin-down mechanism whose effectiveness changes with [Fe/H], a question whose resolution, while intriguing, is well beyond the scope of the current sample.

Second, due to the rapid establishment of the Li dip within clusters by the age of the Hyades/Praesepe (Cummings et al. 2017) and the long-term decline in Li for stars lower in mass than the Li dip (see, e.g., Cummings et al. 2012; Bouvier et al.

2018; Anthony-Twarog et al. 2018, among many others), the stars above the wall have represented a potential pristine indicator of the primordial cluster Li abundance, a clear reference marker against which changes to lower-mass stars could be calibrated, again assuming that the higher-mass stars were minimally affected by processes such as diffusion. It is now apparent that as a cluster ages the Li abundance of the stars above the wall does evolve downward, with the degree of depletion growing with age owing to the declining range in  $v_{\text{rot}}$ , usually well beyond the range defined by the statistical uncertainty in the determination of individual A(Li). Not only does this weaken the value of these stars in defining the original cluster abundance; among the stars above the wall it essentially recreates the Li dip, though at a slower pace and less effectively (D19). The impact on the giant branch is crucial. The masses of the stars reaching the base of the giant branch with severely reduced A(Li) are no longer defined by the mass of the Li wall, but now extend significantly higher. For the numerically rich cluster NGC 6819 at [Fe/H] = -0.04, Li depletion is well underway among stars leaving the main sequence with minimal masses of  $1.57 M_{\odot}$ , even though the Li wall does not occur until one reaches  $1.43 M_{\odot}$ . Clearly, these boundaries will shift downward with decreasing metallicity. Because the level of the Li plateau among lower-mass stars beyond the cool edge of the Li dip on the main sequence will decrease with time (Cummings et al. 2012), the majority of the red giants older than  $\sim$ 2 Gyr will be well below the Li-rich boundary of A(Li) = 1.5, long before they reach the red giant tip and the eventual red giant clump. (Again, the age boundary will depend strongly on [Fe/H]. For example, in NGC 2243, Li-depleted stars above the wall are already leaving the main sequence, despite the fact that the stars defining the Li wall will not begin to populate the subgiant branch until the cluster is 4.1 Gyr old.) Thus, not only is it likely that any lower-mass red clump star with a detectable A(Li) should be classified as Li-rich (Kumar et al. 2020), but a population of lower-mass stars on the firstascent giant branch now tagged as Li-poor may actually show evidence of post-main-sequence Li enhancement prior to arrival at the red giant tip (Twarog et al. 2020; Sun et al. 2020).

We close the investigation of NGC 2243 with a discussion of the broader impact of the delineation of the Li dip with metallicity on our understanding of Galactic Li evolution. The evolution of stars above the wall, i.e., on the warm side of the Li dip, and the metallicity-dependent change in the mass boundaries of the Li dip have subtle but relevant impacts on the interpretation of the Li distribution among field stars. In a recent analysis of the exquisite GALAH database for F and G dwarfs, Gao et al. (2020) identify and analyze over 100,000 stars between [Fe/H] = -3 and +0.5 and  $T_{eff}$  between 5900 and 7000 K. After sorting the stars into three Li categories, "warm" (above the wall), within the Li dip, and "cool" (below the Li dip), the trends with [Fe/H] for the "warm" and "cool" stars were compared. As expected, for stars with [Fe/H] below -1.0, only "cool" stars were present owing to the evolution of "warm" stars off the main sequence by the age typical of these metal-poor dwarfs. The approximately uniform A(Li) for these stars is consistent with Li abundances for stars occupying the Spite plateau (Spite & Spite 1982a, 1982b). Between [Fe/ H] = -1.0 and -0.5, a "warm" sample of 117 stars reappeared and scattered about a mean value of  $A(Li) = 2.69 \pm 0.06$ , statistically identical with the predicted big bang nucleosynthesis value of 2.75. With increasing [Fe/H] above -0.5, A(Li)

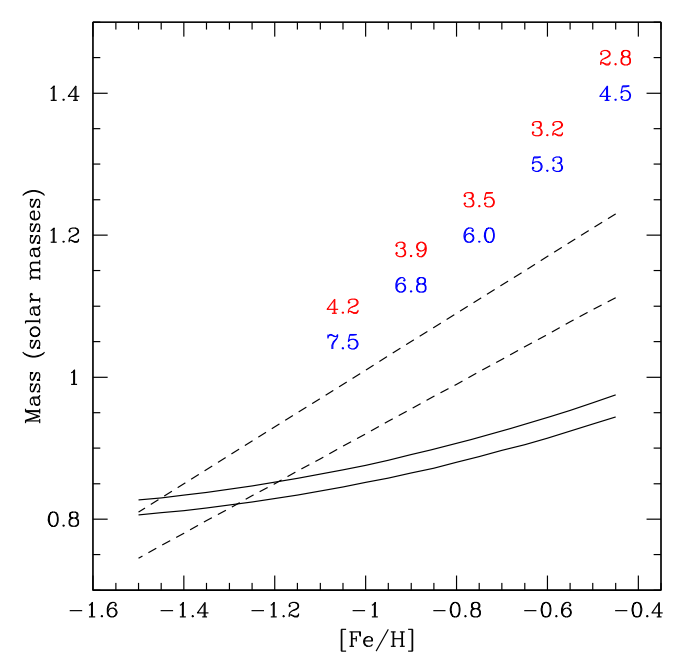


**Figure 12.** Mass range of the Li dip (dashed lines) compared to the mass range for the turnoff stars in a cluster of age 12.5 Gyr (solid lines) as a function of [Fe/H]. Isochrones are assumed to be  $[\alpha/Fe] = 0.4$ . Age (Gyr) at which the Li wall evolves to the subgiant branch is given in blue for metallicity defined as [Fe/H], red for [m/H],  $\alpha$ -enhancement included.

among both the "warm" and the "cool" stars exhibits a steady increase, implying a contribution from Galactic nucleosynthesis superposed on the initial undiluted primordial Li abundance defined by the stars at [Fe/H] = -0.5 to -1.0.

However, the above interpretations of the "warm" star patterns above [Fe/H] = -1.0 are straightforward only if the assumption that these stars retain their initial Li abundance prior to entering the subgiant branch is appropriate. If the trend among the stars above the wall ("warm") with increasing age as defined by the clusters discussed in D19 and extended to [Fe/ H] = -0.5 by NGC 2243 is correct, the mean of the A(Li) distribution of the "warm" stars increasingly underestimates any initial cluster value with increasing age owing to Li depletion triggered by rotational spin-down. Thus, taking the 20 stars above the wall in NGC 2243 as representative of a sample of field "warm" stars at [Fe/H] = -0.5, the mean A(Li) would be  $2.52 \pm 0.06$  (sem), even though the cluster limiting value appears to lie between A(Li) = 2.85 and 3.1. One could minimize this effect if the sample selected is dominated by younger stars of the same mass, but the probability of finding such stars as [Fe/H] declines from -0.5 to -1.0 seems unlikely.

Equally important is the effect of [Fe/H] on the Li dip boundary, i.e., the defining lines for "warm" and "cool" stars. Figure 12 illustrates the competing effects of basic stellar evolution with the potential development of the boundaries of the Li dip. Using the VR isochrones defined with  $[\alpha/Fe]$  set at +0.4, the mass range of the stars populating the CMD turnoff at an age of 12.5 Gyr with decreasing [Fe/H] is shown as a pair of solid lines. The mass range of the turnoff is defined from the bluest point of the main-sequence CMD to a position 0.10 mag redder in B-V, the latter boundary selected to avoid stars normally classified as subgiants. The masses are set using isochrones with an age of 12.5 Gyr across the board. Clearly, shifting the models to younger ages would slide the relations to

a systematically higher mass. By contrast, the dashed lines show the mass boundaries of the Li dip, created by simple extrapolation of the linear trends defined by multiple clusters from [Fe/H] = -0.5 (NGC 2243) to +0.45 (NGC 6253) (Cummings et al. 2012). We note that the lower-mass boundary of the Li dip as applied in Figure 12 is not defined by the mass of the cool star plateau (Cummings et al. 2012; François et al. 2013) beyond the Li dip, but the mass where A(Li) initially rises to a level of consistent detectability. In the case of NGC 2243, this shifts the lower-mass boundary from  $1.03\,M_\odot$  (François et al. 2013) to  $1.09\,M_\odot$  (Figure 6).

As expected, the simplistic extrapolation of the Li dip mass range crosses the globular cluster mass trend between [Fe/ H] = -1.25 and -1.50, in contradiction with the absence of the Li dip within globular cluster CMDs and the existence of the Spite plateau. An obvious solution to the contradiction is that the mass/metallicity slope flattens below [Fe/H] = -0.5, preventing the Li dip from ever crossing the evolutionary trend with lower metallicities except among younger isochrones. Because the mass/metallicity relation is based on clusters with scaled-solar abundances, it is possible that it is inapplicable to stars/clusters with enhanced  $[\alpha/Fe]$ , i.e., metallicity should refer to [m/H] rather than [Fe/H]. If the typical star below [Fe/H] = -0.5 has  $[\alpha/Fe] = +0.4$ , as assumed for the isochrones, the mass boundaries should be boosted by as much as 0.14 to  $0.16 M_{\odot}$  at the "cool" and "warm" boundaries, pushing the crossover of the two trends to [Fe/H] below -2.5.

The relevance of these qualitative trends is illustrated by the sequence of ages (Gyr) plotted as a function of [Fe/H] in Figure 12. The blue terms define the last age at which a star of the given [Fe/H] can be found on the "warm" side of the Li dip, assuming that the mass boundary is defined by extrapolation of the linear trend above [Fe/H] = -0.5, not including the possible role of  $[\alpha/\text{Fe}] = +0.4$  within the metallicity. The red points define the same age marker but include the enhanced  $\alpha$ elements in the mass boundary determination, i.e., M/ $M\odot = -0.4^* [m/H] + constant$ , for the "warm" stars. Two points are immediately obvious. In either case, there is a significant age bias in the selection of observable stars. The more metal-rich the star, the younger it has to be to be included in a "warm" star sample. Second, mechanisms used to alter the slope of the mass/metallicity relation by making it shallower or by shifting it to higher mass limits with metallicity, as done via alteration of the definition of metallicity in Figure 12, invariably move the age boundary for the "warm" stars to a younger age, creating an even more extreme selection bias within any "warm" star sample from the field.

The selection bias due to age limitations for populating the "warm" side of the Li dip, coupled with Li depletion among "warm" stars prior to entering the subgiant branch, has already been seen among stars at the metal-rich end of the scale. A number of studies have claimed that the limit to A(Li) among stars of supersolar metallicity declines as [Fe/H] increases (see, e.g., Fu et al. 2018; Guiglion et al. 2019; Bensby et al. 2020; Stonkutė et al. 2020). This apparent trend is readily understood if the Li dip boundaries plotted in Figure 12 are extended to [Fe/H] = +0.5, using isochrones with scaled-solar abundances. From our mass/[Fe/H] relation, at [Fe/H] = -0.04 and +0.43 the mass boundaries for the wall are located at 1.42 and  $1.61 M_{\odot}$ , respectively. Using the same definition as earlier, these mass boundaries enter the subgiant branch at an age of

3.1 and 2.4 Gyr, respectively. The former metallicity is representative of NGC 6819 (age =  $2.3 \pm 0.1$  Gyr; D19), with a spread of A(Li) among its warm stars of 1.4 dex. The latter metallicity is representative of NGC 6253 (Anthony-Twarog et al. 2010; Cummings et al. 2012; age =  $3.0 \pm 0.4$  Gyr). Stars leaving the turnoff in NGC 6253 are clearly emerging from within the Li dip; of the 12 stars on the warmer side of the Li dip and across the subgiant branch, only 2 have detections, and both of these are below A(Li) = 2.1, even though the stars populating the cool star plateau beyond the Li dip almost reach A(Li) = 2.8.

If the spreads in A(Li) among the "warm" stars in NGC 2243 and NGC 6819 seen prior to the evolution of their walls onto their subgiant branch are typical of clusters of higher metallicity of comparable "Li age," one would expect to see a significant range in A(Li) among "warm" stars at [Fe/H] near +0.4 between the ages of approximately 1.6 and 2.3 Gyr. Thus, for supersolar metallicity the initial cluster A(Li) would only remain detectable as a mean value among the "warm" stars at ages below  $\sim 1.6 \,\mathrm{Gyr}$ , with the boundary rising as [Fe/H] declines to solar. For ages between this boundary and the age when the wall enters the subgiant branch, the initial A(Li) may still be detectable, but only as an upper limit to the sample. This pattern is totally consistent with the Li analysis of 18 clusters, 7 of which have [Fe/H] > 0, by Randich et al. (2020). With one cluster at 1.4 Gyr and all others at 1.0 Gyr or less, Randich et al. (2020) find no decrease in A(Li) with increasing [Fe/H]. In fact, the clusters with higher metallicity have the highest A(Li).

NSF support for this project was provided to B.J.A.-T. and B.A.T. through NSF grant AST-1211621 and to C.P.D. through NSF grants AST-1211699 and AST-1909456. The assistance of KU undergraduate Steven Smith was instrumental in the early stages of this project; Dr. Donald Lee-Brown assisted with observations and development of the ANNA code. This research has made use of the WEBDA database, operated at the Department of Theoretical Physics and Astrophysics of the Masaryk University. This research has made use of the services of the ESO Science Archive Facility and is based on observations collected at the European Southern Observatory under the public Gaia ESO Survey Program.

Facility: WIYN: 3.5 m.

Software: IRAF Tody (1986), ANNA Lee-Brown (2017, 2018), MOOG Sneden (1973), LACOSMIC van Dokkum (2001).

#### ORCID iDs

Barbara J. Anthony-Twarog https://orcid.org/0000-0001-8841-3579

Constantine P. Deliyannis https://orcid.org/0000-0002-3854-050X

Bruce A. Twarog https://orcid.org/0000-0001-5436-5206

## References

Anthony-Twarog, B. J., Atwell, J., & Twarog, B. A. 2005, AJ, 129, 872, (ATAT)

Anthony-Twarog, B. J., Deliyannis, C. P., Rich, E., & Twarog, B. A. 2013, ApJL, 767, L19

Anthony-Twarog, B. J., Deliyannis, C. P., & Twarog, B. A. 2014, AJ, 148, 51
Anthony-Twarog, B. J., Deliyannis, C. P., & Twarog, B. A. 2016, AJ, 152, 192
Anthony-Twarog, B. J., Deliyannis, C. P., & Twarog, B. A. 2020, AJ, 160, 75, (Paper I)

```
Anthony-Twarog, B. J., Deliyannis, C. P., Twarog, B. A., Croxall, K. V., &
   Cummings, J. 2009, AJ, 138, 1171
Anthony-Twarog, B. J., Deliyannis, C. P., Twarog, B. A., Cummings, J. D., &
  Maderak, R. M. 2010, AJ, 139, 2034
Anthony-Twarog, B. J., Lee-Brown, D. B., Deliyannis, C. P., & Twarog, B. A.
   2018, AJ, 155, 138
Bensby, T., Feltzing, S., & Yee, J. 2020, A&A, 634, A130
Bergbusch, P. A., VandenBerg, D. A., & Infante, L. 1991, AJ, 101, 2102
Boesgaard, A. M., & Tripicco, M. J. 1986, ApJL, 302, 49
Bonifazi, F., Fusi Pecci, F., Romeo, G., & Tosi, M. 1990, MNRAS, 245, 15
Bouvier, J., Barrado, D., Moraux, E., et al. 2018, A&A, 613, A63
Bruntt, H., Basu, S., Smalley, B., et al. 2012, MNRAS, 423, 122
Cameron, A. C., & Reid, N. 1987, MNRAS, 224, 821
Cantat-Gaudin, T., Jordi, C., Vallenari, A., et al. 2018, A&A, 618, 93
Carlberg, J. K., Smith, V. V., Cunha, K., et al. 2015, ApJ, 802, 7
Casali, G., Magrini, L., Tognelli, E., et al. 2019, A&A, 629, A62
Cummings, J. D., Deliyannis, C. P., Anthony-Twarog, B. J., Twarog, B. A., &
   Maderak, R. M. 2012, AJ, 144, 137
Cummings, J. D., Deliyannis, C. P., Maderak, R. M., & Steinhauer, A. 2017,
    J, 153, 128
Deliyannis, C. P., Anthony-Twarog, B. J., Lee-Brown, D. B., & Twarog, B. A.
   2019, AJ, 158, 163, (D19)
Deliyannis, C. P., Steinhauer, A., & Jeffries, R. D. 2002, ApJL, 577, L39
François, P., Pasquini, L., Biazzo, K., Bonifacio, P., & Palsa, R. 2013, A&A,
  552, A136, (FR13)
Friel, E. D., & Janes, K. A. 1993, A&A, 267, 75
Friel, E. D., Janes, K. A., Tavarez, M., et al. 2002, AJ, 124, 2693
Fu, X., Romano, D., Bragaglia, A., et al. 2018, A&A, 610, A38
Gaia Collaboration, Brown, A. G. A., Vallenari, A., et al. 2018a, A&A, 616,
   A1, (DR2)
Gao, Q., Lind, L., Amarsi, A. M., et al. 2020, MNRAS, 497, L30
Gao, Q., Shi, J.-R., Yan, H.-L., et al. 2019, ApJS, 245, 33
Graham, J. A. 1982, PASP, 94, 244
Gratton, R. G. 1982, AJ, 257, 640
Gratton, R. G., & Contarini, G. 1994, A&A, 283, 911
Green, G. M., Schlafly, E. F., Zucker, C., Speagle, J. S., & Finkbeiner, D. P.
   2019, ApJ, 887, 93
Guiglion, G., Chiappini, C., Romano, D., et al. 2019, A&A, 623, A99
Handberg, R., Brogaard, K., Miglio, A., et al. 2017, MNRAS, 472, 979
Hill, V., & Pasquini, L. 2000, in IAU Symp. 198, The Light Elements and
   Their Evolution, ed. L. Da Silva, J. R. de Medeiros, & M. Spite (San
   Fransisco, CA: ASP), 293, (HP)
Houdashelt, M. L., Frogel, J. A., & Cohen, J. G. 1992, AJ, 103, 163
```

```
Jackson, R. J., Jeffries, R. D., Wright, N. J., et al. 2020, MNRAS, 496, 4701
Jacobson, H. R., Friel, E. D., & Pilachowski, C. A. 2011, AJ, 141, 58
Jayasinghe, T., Stanek, K. Z., Kochanek, C. S., et al. 2019, MNRAS, 486, 1907
Kaluzny, J., Krzemińksi, W., & Mazur, B. 1996, A&A, 118, 303
Kaluzny, J., Krzemińksi, W., Thompson, I. B., & Stachowski, G. 2006a, AcA,
Kaluzny, J., Pych, W., & Rucinski, S. M. 2006b, AcA, 56, 237
Kovalev, M., Bergemann, M., Ting, Y.-S., & Rix, H.-W. 2019, A&A, 628, 54
Kumar, Y. B., Reddy, B. E., Campbell, S. W., et al. 2020, NatAs, 4, 1059
Kurucz, R. L. 1995, in IAU Symp. 149, The Stellar Populations of Galaxies,
  ed. B. Barbuy & A. Renzini (Dordrecht: Kluwer), 225
Landolt, A. U. 1983, AJ, 88, 439
Lee-Brown, D. 2018, PhD Thesis, Univ. of Kansas
Lee-Brown, D., Anthony-Twarog, B. J., Deliyannis, C. P., Rich, E., &
  Twarog, B. A. 2015, AJ, 149, 121
Lee-Brown, D. B. 2017, Artificial Neural Network Abundances (ANNA),
  v0.1.0, Zenodo, doi:https://doi.org/10.5281/zenodo.1043585
Magrini, L., Randich, S., Kordopatis, G., et al. 2017, A&A, 603, A2
Mermilliod, J.-C., Mayor, M., & Udry, S. 2008, A&A, 485, 303
Minitti, D. 1995, A&AS, 113, 299
Netopil, M., Paunzen, E., Heiter, U., & Soubiran, C. 2016, A&A, 585, 150
Ramírez, I., & Meléndez, J. 2005, ApJ, 626, 465
Randich, S., Pasquini, L., Franciosini, L., et al. 2020, A&A, 640, L1
Riess, A. G., Casertano, S., Yuan, W., et al. 2018, ApJ, 861, 126
Schlafly, E. F., & Finkbeiner, D. P. 2011, ApJ, 737, 103
Schlegel, D. J., Finkbeiner, D. P., & Davis, M. 1998, ApJ, 500, 525
Shappee, B. J., Prieto, J. L., Grupe, D., et al. 2014, ApJ, 788, 48
Sneden, C. 1973, ApJ, 184, 839
Spite, F., & Spite, M. 1982a, A&A, 115, 357
Spite, M., & Spite, F. 1982b, Natur, 297, 483
Stassun, K. G., & Torres, G. 2018, ApJ, 862, 61
Steinhauer, A. 2003, PhD thesis, Indiana Univ.
Stonkutė, E., Chorniy, Y., Tautvaišienė, G., et al. 2020, AJ, 159, 90
Sun, Q., Deliyannis, C. P., Twarog, B. A., et al. 2020, AJ, submitted
Tody, D. 1986, Proc. SPIE, 627, 733
Twarog, B. A., Anthony-Twarog, B. J., Deliyannis, C. P., & Steinhauer, A.
  2020, MmSAI, 91, 74
Twarog, B. A., Ashman, K. M., & Anthony-Twarog, B. J. 1997, AJ, 114, 2556
van Dokkum, P. G. 2001, PASP, 113, 1420
VandenBerg, D. A., Bergbusch, P. A., & Dowler, P. D. 2006, ApJS, 162, 375
Waters, C. Z., & Hollek, J. K. 2013, PASP, 215, 1164
Wenger, M., Ochsenbein, F., Egret, D., et al. 2000, A&AS, 143, 9
Zinn, J. C., Pinsonneault, M. H., Huber, D., & Stello, D. 2019, ApJ, 878, 136
```